

Contents — T

| | |
|---|------|
| Water Cycling in the North Polar Region of Mars <i>L. K. Tamppari, M. D. Smith, A. S. Hale, and D. S. Bass</i> | 3121 |
| Mars: Updating Geologic Mapping Approaches and the Formal Stratigraphic Scheme <i>K. L. Tanaka and J. A. Skinner Jr.</i> | 3129 |
| Igneous and Aqueous Processes on Mars: Evidence from Measurements of K and Th by the Mars Odyssey Gamma Ray Spectrometer <i>G. J. Taylor, W. Boynton, D. Hamara, K. Kerry, D. Janes, J. Keller, W. Feldman, T. Prettyman, R. Reedy, J. Brückner, H. Wänke, L. Evans, R. Starr, S. Squyres, S. Karunatillake, O. Gasnault, and the Odyssey GRS Team</i> | 3207 |
| The Microscope for the Beagle 2 Lander on ESA's Mars Express <i>N. Thomas, S. F. Hviid, H. U. Keller, W. J. Markiewicz, T. Blümchen, A. T. Basilevsky, P. H. Smith, R. Tanner, C. Oquest, R. Reynolds, J.-L. Josset, S. Beauvivre, B. Hofmann, P. Ruffer, C. T. Pillinger, M. R. Sims, D. Pullan, and S. Whitehead</i> | 3015 |
| The South Polar Residual Cap of Mars: Landforms and Stratigraphy <i>P. C. Thomas</i> | 3058 |
| Carbonates on Mars: Probable Occurrences, Spectral Signatures, and Exploration Strategies <i>B. J. Thomson and P. H. Schultz</i> | 3229 |
| Great Martian Dust Storm Precursor? <i>J. E. Tillman</i> | 3164 |
| Temporal and Spatial Distribution of Seasonal CO ₂ Snow and Ice <i>T. N. Titus and H. H. Kieffer</i> | 3273 |
| Correlation of Neutron-sensed Water Ice Margins with Topography Statistics <i>R. L. Tokar, M. A. Kreslavsky, J. W. Head III, W. C. Feldman, K. R. Moore, and T. H. Prettyman</i> | 3181 |
| Low-Temperature Aqueous Alteration on Mars: Insights from the Laboratory <i>N. J. Tosca, S. M. McLennan, D. H. Lindsley, and M. A. A. Schoonen</i> | 3178 |
| The Beagle 2 Environmental Sensors: Intended Measurements and Scientific Goals <i>M. C. Towner, T. J. Ringrose, M. R. Patel, D. Pullan, M. R. Sims, S. Haapanala, A.-M. Harri, J. Polkko, C. F. Wilson, and J. C. Zarnecki</i> | 3024 |
| Convective Plumes as 'Columns of Life' <i>B. J. Travis</i> | 3230 |

WATER CYCLING IN THE NORTH POLAR REGION OF MARS. L. K. Tamppari¹, M. D. Smith², A. S. Hale³, and D. S. Bass³, ¹NASA Jet Propulsion Laboratory (4800 Oak Grove Drive, Pasadena, CA 91109 leslie.k.tamppari@jpl.nasa.gov), ²NASA Goddard Space Flight Center (Michael.D.Smith.1@gsfc.nasa.gov), ³NASA Jet Propulsion Laboratory (MS 264-235, 4800 Oak Grove Drive, Pasadena, CA 91109 amy.s.hale@jpl.nasa.gov), ⁴NASA Jet Propulsion Laboratory (MS T1722, 4800 Oak Grove Drive, Pasadena, CA 91109 deborah.s.bass@jpl.nasa.gov).

Introduction: The Martian water cycle is one of the three annual cycles on Mars, dust and CO₂ being the other two. Despite the fact that detailed spacecraft data, including global and annual coverage in a variety of wavelengths, have been taken of Mars spanning more than 25 years, there are many outstanding questions regarding the water cycle.

There is very little exposed water on Mars today, in either the atmosphere or on the surface [1] although there is geological evidence of catastrophic flooding and continuously running water in past epochs in Mars' history [2] as well as recent (within about 10,000 years ago) evidence for running water in the form of gullies [3]. While there is little water in the atmosphere, water-ice clouds do form and produce seasonal clouds caused by general circulation and by storms [5-8]. These clouds may in turn be controlling the cycling of the water within the general circulation [e.g., 6].

The north polar cap region is of special interest as the residual cap is the main known reservoir of water on the planet today. The south polar residual cap may contain water, but presents a CO₂ ice covering, even during southern summer. This hemispheric dichotomy is unexplained and is especially puzzling due to the fact that the Martian southern summer is much warmer (due to Mars' eccentricity) than the northern summer. Recently, water has been found in the top meter of the surface in both the northern and southern high latitude regions [e.g. 8-9] indicating an even greater amount of water on Mars than previously known.

Background: In order to better understand the current climate of Mars, we seek to understand atmospheric water in the north polar region. Our approach is to examine the water transport and cycling issues within the north polar region and in/out of the region on seasonal and annual timescales. Viking Mars Atmospheric Water Detector (MAWD) data showed that water vapor increased as the northern summer season progressed and temperatures increased, and that vapor appeared to be transported southward [10]. However, there has been uncertainty about the amount of water cycling in and out of the north polar region, as evidenced by residual polar cap visible brightness changes between one Martian year (Mariner 9 data) and a subsequent year (Viking data). These changes were originally thought to be interannual variations in the amount

of frost sublimed based on global dust storm activity [10-12]. However, Viking thermal and imaging data were re-examined and it was found that 14-35 pr □m of water -ice appeared to be deposited on the cap later in the summer season [14], indicating that some water may be retained and redistributed within the polar cap region. This late summer deposition could be due to adsorption directly onto the cap surface or due to snowfall. The possibility that some of the water is seasonally sequestered in water-ice clouds and may allow later precipitation had not been previously considered. We address these issues by examining water vapor and water-ice clouds in the north polar region of Mars during the north spring and summer period.

Method:

Water-ice clouds. Water-ice clouds, in the north polar region, have previously been tentatively identified in the Viking era using the Infrared Thermal Mapper (IRTM) data [14] and in the Mars Global Surveyor (MGS) era using the Thermal Emission Spectrometer (TES) data ([15] and M. Smith, pers. comm., 2001). The Viking data provides only nadir pointed data, which necessitates separating the surface contribution from the atmospheric contribution. The technique used relies on the water-ice absorption feature at 11-microns. Specifically, it uses the 11- and 20-micron channels of the IRTM instrument along with a surface model to accurately remove the surface contribution [4]. For the Viking time frame, we are restricted to ice free surfaces and therefore do not see the entire north polar cap region throughout the spring and summer season.

With the MGS TES data, there exist both limb- and nadir-pointed data. The nadir-pointed data retrievals are currently performed for water ice clouds only over surfaces above 220 K (M. Smith, pers. comm.). The surface is colder than 220 K northward of 60° N at L_s=0°, but this latitude limit moves gradually northward as spring progresses, reaching the pole just before L_s=90°. The TES limb data do not have any complications due to cold surface temperatures. Therefore, water-ice clouds can be identified throughout the Martian season, even over the seasonal and residual polar cap.

MGS TES data over the poles are taken much more frequently than over other areas of the planet due to the nature of the orbit. The nominal TES observing sequence has limb-geometry observations taken every 10 degrees in latitude. The orbit of MGS is such that over a 2-sol period (approximately 1 degree of L_s), approximately 24 orbits of Mars are made with tracks spaced roughly evenly every 15 degrees in longitude. Therefore, in the polar region, while not as dense as the nadir-geometry observations, the limb-geometry observations help to fill out the data set and provide an additional cut through the atmosphere from which to identify clouds and vapor. The limb data also offer the possibility to detect the cloud heights as there are multiple spectra over the vertical range.

Water vapor. Smith *et al.* [17] have performed retrievals for the column-integrated abundance of water vapor using the rotational water vapor bands at 220-360 cm^{-1} . Atmospheric temperatures are first retrieved using the 15- μm CO_2 band (Conrath *et al.*, 2000). Next, a forward radiative transfer computation is used to find the column-integrated water abundance that best fits the observed water vapor bands. At this time water is assumed to be well-mixed up to the condensation level and then zero above that. A total of six water vapor bands between 220 and 360 cm^{-1} are observed in TES spectra and the widths and relative depths of all six bands are very well fit by the synthetic spectra. Because the spectral signature of water vapor is spectrally very distinct from those of dust and water-ice, we can easily separate the relative contributions from each component (dust, water-ice, and water vapor) on a spectrum-by-spectrum basis.

Recent analysis with MGS TES data has shown evidence for water vapor "pulses" as the seasonal north polar cap sublimates [15]. This could be linked to the previous late-summer season deposition, discussed above. Additionally, there may be some differences in the details of the water vapor as a function of latitude and season between the Viking era and the current era. Any such differences would help identify and characterize the degree of interannual variability in the water vapor. There is also indication of latitudinal water vapor transport as a function of season seen through longitudinally averaged water vapor [16 and Figure 1]. We will present our latest results on water vapor transport, spatially and temporally.

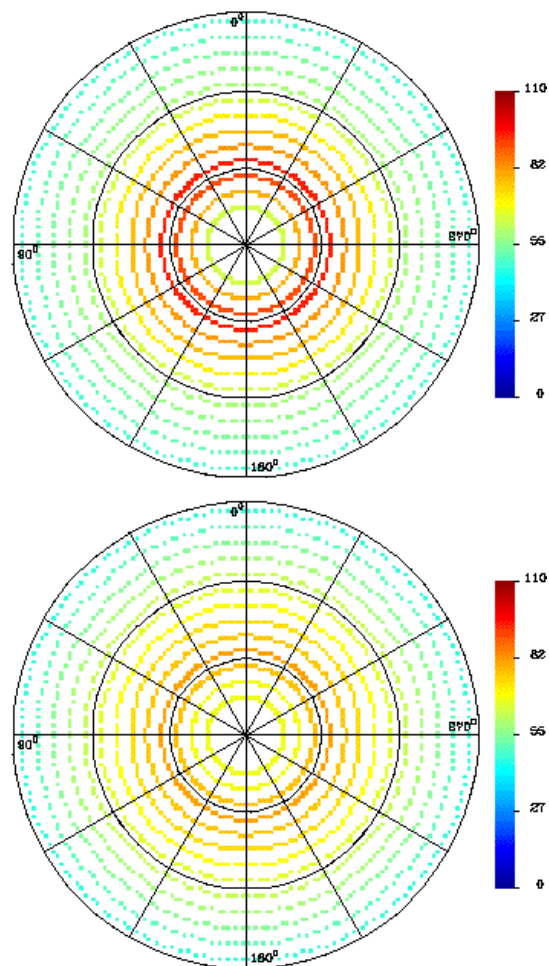


Figure 1. Longitudinally averaged water vapor as a function of latitude for $L_s=115^\circ$ (top) and $L_s=117^\circ$ (bottom). The amount of water vapor in the centermost ring (highest latitude ring) shows about a 15 pr micron enhancement in $2^\circ L_s$, while the 3rd and 4th rings from the center show a decrease in vapor amount.

Dust. Dust in the north polar region can play an important role in the water cycling story in a couple of ways. One, by acting as cloud condensation nuclei, dust may allow water-ice clouds to form and could potentially cause gravitational settling and sequestering of the water. Two, dust may be sufficiently radiatively active to prohibit clouds from forming and potentially allowing a greater degree of water vapor transport out of the polar region. The MGS TES instrument also spans the wavelength region over which Martian dust is absorbing, allowing its retrieval.

Surface Temperature. The north polar region surface temperature during the northern polar season can be compared to the Viking era to further elucidate potential interannual differences and to understand the vapor, water-ice, and dust retrievals. MGS TES is also

capable of measuring the surface temperature. Surface temperatures can confirm that carbon dioxide is not present on the cap surface, implying that any brightening is likely water ice.

Intercorrelation of data: To date, there has been no comprehensive study to understand the partitioning of water into vapor and ice clouds, and the associated effects of dust and surface temperature in the north polar region. Ascertaining the degree to which water is transported out of the cap region versus within the cap region will give much needed insight into the overall story of water cycling on a seasonal basis. In particular, understanding the mechanism for the polar cap surface albedo changes would go along way in comprehending the sources and sinks of water in the northern polar region. We approach this problem by examining TES atmospheric and surface data acquired in the northern summer season and comparing it to Viking data when possible. Because the TES instrument spans the absorption bands of water vapor, water ice, dust, and measures surface temperature, all three aerosols and surface temperature can be retrieved simultaneously. This presentation will show our latest results on the water vapor, water-ice clouds seasonal and spatial distributions, as well as surface temperatures and dust distribution which may lend insight into where the water is going.

References: [1] Keiffer H. H. et al. (1976) *Science*, 194, 1341-1344 [2] Carr, M. H. (1998) *Water on Mars* [3] Malin M. C. and Edgett, K. S. (2001) *JGR* 106, 23429-23570. [4] Tamppari, L. K. et al. (2000) *JGR* 105, 4087-4107. [5] Smith, M. D et al. (2001) *JGR* 107, 5115-5134. [6] Richardson, M. I. et al. (2002) *JGR* 107, 5064-5093. [7] Hollingsworth, J. L. et al. (1997), *Nature* 380, 413-416. [8] Feldman W. C. et al., (2002) *Science* 297, 75-78 [9] Boynton W. V. et al., (2002) *Science* 297, 81-85 [10] Jakosky, B. M. (1985), *Space Sci. Rev.* 41, 131-200. [11] James P. B. and Martin L. (1985) *Bull. Amer. Astron. Soc.*, 17, 735. [12] Kieffer H. H. (1990) *JGR*, 96, 1481-1493. [13] Bass D. S. et al. (2000) *Icarus*, 144, 382-396. [14] Tamppari L. K. and Bass D. S. (2000) *2nd Mars Polar Conf.* [15] Tamppari L. K. et al. (2002) *Bull. 34th Am. Astron. Soc.*, 845. [16] Tamppari L. K. et al. (2003) *LPSC XXXIV*, Abstract #1650. [17] Smith M. D. et al. (2000), *Bull. AAS*, 32(3), 1094.

MARS: UPDATING GEOLOGIC MAPPING APPROACHES AND THE FORMAL STRATIGRAPHIC SCHEME. K. L. Tanaka and J. A. Skinner, Jr., U.S Geological Survey, 2255 N. Gemini Dr., Flagstaff, AZ 86001; ktanaka@usgs.gov.

Introduction: At the Fourth Mars Conference in 1989, Tanaka reviewed the stratigraphy and geologic history of Mars that had emerged based on systematic geologic mapping of the planet's surface using Viking data [1]. This review looked at the stratigraphic column for Mars and assessed the global geologic history in terms of impact, fluvial, periglacial, aeolian, volcanic, and tectonic processes. Many significant new studies using Mars Global Surveyor (MGS) and now Mars Odyssey (MO) data are showing some important new insights and discoveries that are altering and deepening previous understandings. If we were to illustrate the current state of the science, we might compare it to a loose-leaf notebook in which pages are rapidly being added, removed, and rewritten, with plenty of room remaining. Much of the flux is due to new data, of course, but also much can be attributed to the re-examination of basic assumptions and approaches and our ability to employ ever more powerful computer techniques. Here, we will attempt to review, based on our experience, the areas where the most change seems to be occurring, what prospects we face in the immediate future, and where caution needs to be exercised.

Geologic Mapping Approaches: The fundamental technique for reconstructing the history of planetary surfaces is geologic mapping. Maps portray the distribution of rock units and surface features as they developed through time, based on morphologic relative-age indicators including superposition and cross-cutting relations as well as crater-density determinations where possible, as on Mars.

Previous Methods and Their Shortcomings. Generally, map units for Mars have been based on morphology, albedo, relative ages, and topography using Mariner 9 and Viking images. These data have proved to be valuable but challenging to map with, because of inconsistencies in or problems with resolution, atmospheric opacity, solar illumination, and image locating. MGS MOLA data have been extremely valuable in providing improved topographic and morphologic views over much of the planet's surface. However, cross-track spacing is locally quite large in the equatorial region and above 87° latitudes, where off-nadir pointing was required. New, largely nadir visible and thermal infrared images of the surface by MGS MOC and MO THEMIS provide higher resolution and different wavelength views of the surface. MOC NA images reveal close-up views of morphology and albedo

features at meters to tens of meters scales such as rock layers and craters [2]. Depending on scale, these new data sets will likely justify revised mapping of Mars.

While the prospects for new results detailing the geologic history of Mars are bright based on new data alone, improved mapping methods will also be significant. Since the days of systematic geologic mapping using Mariner 9 data, Mars geologic map units have been characterized and named on the basis of morphologic and albedo features that we now (as well as previously) realize represent secondary features related to surface modification and tectonic deformation (rather than to the primary origin of the unit). Examples of secondary descriptors in unit names include "ridged," "lineated," "channel," "dissected," "cratered," "mottled," "etched," "knobby," "smooth," and "rough." Albedo seems to be a consistently mappable characteristic only where the surface is free from dust due to recent atmospheric activity; (e.g., polar residual ice, which varies annually in extent), or where the dust and soil themselves are being mapped. However, much of the planet is covered by a shifting mantle of dust as indicated by high albedo and low thermal inertia data.

Some units have composite signatures of significance, but the unit name may focus on only one item. Thus, "knobby material" usually signifies knobs of one material surrounded by plains-forming material of another material type and age. Finally, unit descriptor terms usually have relative and thus imprecise meaning; as an example, a "smooth" surface at small scale may be characterized as "rough" at larger scales. Thus morphology, albedo, and other surficial data must be used with caution, if at all, in defining map units. In many cases, it may be difficult to determine whether particular signatures are primary or secondary (e.g., the high albedo of a rough surface could be primary or it may represent a coating of much younger, high-albedo aeolian material).

The use of secondary features in unit names and definitions engenders the misconception that the secondary features are either primary or at least about the same age as the material unit being mapped. Even worse, mappers may be inclined to map material unit contacts on the basis of the presence or absence of those features without carefully testing this approach. These issues have been addressed in the case of photo-geologic mapping of planetary surfaces marked by tectonic structures [3], which is particularly applicable

to Venus and outer planet satellites. The Moon, Mercury and Mars also have surfaces displaying sufficient ranges in crater densities to provide an effective tool in relative-age dating. Mars is an especially complex case, because it also has experienced significant erosion. Thus determining the relative ages of secondary features requires special care. For example, feature terminations (e.g., of grabens or valleys) may represent either the original, full extent of the features or the extent to where obliteration has occurred due to resurfacing by erosion, degradation, or burial by younger material. To discriminate between these possibilities, additional evidence is required such as embayment by younger material. It is insufficient to rely solely on a lower crater density where the features are missing, because erosion or the former presence of mantles may account for a lower crater density and not younger material.

While it may be particularly evident that many morphologic and albedo signatures may be secondary and thus should not be included in map-unit definitions and names, we also see a danger in using terrain descriptors, such as “highlands,” “plains,” “hilly,” “floor,” and “basement.” Such descriptors force the mapper to pigeonhole outcrops on the basis of terrain, although geologic units may actually occur in multiple terrain settings. Furthermore, terrain descriptors do not make sense in cross section, as in “ridged plains material” that may make up kilometers-thick sequences of flows exposed in the walls of Valles Marineris and Kasei Valles or as in “channel floor material” actually made up of scoured older material. In some cases, but not generally, mappers have called these units “geomorphic units,” recognizing they represent younger surfaces rather than younger materials. However, such maps suffer from the added complexity of not being fully geologic maps.

Another shortcoming in much of the previous geologic mapping of Mars has been the nature of contact relations among map units, which was not studied carefully, not documented adequately, and/or not mapped in detail using multiple contact types. Thus the reader is left uninformed about the specific inferences and their associated uncertainties used in defining map units, in mapping contacts, and in determining relative-age relations between units. Many contacts among Noachian materials and younger plains-forming materials in particular have been described as gradational, which could mean gradational in morphology, age, lithology, provenance, emplacement processes, etc., with adjacent units.

Improved Mapping Approaches. We are implementing some significant new approaches in our geologic map of the northern plains of Mars (in progress)

in order to overcome the aforementioned shortcomings. These approaches may need further refinement and thus should be regarded as tentative.

First, we are not using morphology, albedo, terrain, or any other physical characteristics in map-unit names. Following terrestrial methods, units are named strictly after associated geographic terms (e.g., *Vastitas Borealis* Formation). They may also be distinguished by geochronologic period (e.g., Noachian), relative stratigraphic position (e.g., upper, lower, 1, 2, 3), and/or lateral facies (interior, exterior, marginal, proximal, distal).

Second, we define map units only by their apparent primary features, and secondary features are discussed only as they relate to unit character. Examples of the latter include inferences such as yardangs indicative of friable materials and steep scarps suggestive of resistant material. In addition to lithologic (rock-stratigraphic units), we recommend also mapping unconformity-bounded units (UBUs) [4] (or allostratigraphic units [5]) that discriminate material units by relative age, wherever a significant hiatus can be demonstrated in the geologic record. Also, these units may consist of multiple lithologies, useful when an intimate mixture of diverse lithologies may prove to be impractical to map but all have a geologic and temporal association. Thus lobate materials of diverse, mixed morphologies in Utopia Planitia may include lava and ash flows, lahars, and mudflows of diverse lithology but all related to the same period of volcanism and erosion of the western flank of the Elysium rise as defined by stratigraphic relations and crater counts. Another example would be two sets of overlapping lava flows in which the older set is faulted by grabens and the younger set buries the grabens. While UBUs have been used in essence in previous mapping to some degree, the lack of their formal recognition as a legitimate unit type has resulted in inconsistency in their application.

Third, we avoid discriminating units having considerable overlap in both character and age. We thus have not separated out both Late and Middle Noachian highland units in our northern plains mapping (as in the cratered and subdued units of the plateau sequence as mapped previously [6]). Most Noachian surfaces show high variability in crater densities and terrain ruggedness, but few display strong morphologic indications of embayment and overlap relations that relate to distinctive epochs. We only have mapped within ~300 km of the highland/dichotomy boundary; and Late Noachian materials appear to occur elsewhere, such as material covering Thaumasia Planum south of Coprates Chasma [7].

Fourth, we attempt to lump or split units based on geologic associations at map scale. This is not a new

approach, but implementing it has improved now that MOLA and other new data better define topographic and other associations for provenance of deposits and source regions of volcanic flows.

Fifth, we more carefully define and map contact types according to USGS standards [8], including: certain, approximate, gradational, inferred, and inferred approximate. However, the USGS guidelines seem to be poorly defined, so we have provided our own: *Certain* denotes a precise contact between well-characterized material units, whereas *approximate* contacts are less precisely mapped due to data quality, subtlety of the contact, and/or secondary surface modification. *Gradational* contacts are used around composite units made up of intimate mixtures (at map scale) of older materials and their apparent erosional products, such as knobs of older material surrounded by younger slope material; such units grade with adjacent, continuous outcrops of both the older material and younger plains-forming material at the base of the knobs. *Inferred* contacts are used when the material distinctiveness between the map units is subject to question. An example is the contact between what we are mapping as the interior and marginal members of the Vastitas Borealis Formation. The interior member may be simply a different morphologic expression of the same material and emplacement age as the marginal member, or it may represent material of the marginal member that was later pervasively and intensely reworked. Digital mapping of line work greatly facilitates the drafting and editing of multiple contact types.

The Formal Martian Stratigraphic Scheme: Surprisingly, the scheme initially introduced by Scott and Carr [9] from Mariner 9 based global geologic mapping and later refined using Viking global geologic mapping results and crater-density data [1], has fairly well withstood the test of time and dozens of local and regional studies in the assigning of relative-ages based on crater densities and stratigraphic relations. However, aspects of the scheme are either flawed or need revisiting.

Referents and Time-Stratigraphic Units. The present stratigraphic scheme for Mars is based on the formal time-stratigraphic methodology developed for Earth [5]. Time-stratigraphic (or chronostratigraphic) units define stratigraphic position and are based on rock units that can be used to define a specific period of geologic time; the base of the unit represents the beginning of the period. Time-stratigraphic units form Systems and their subdivisions, Series, and their chronological equivalents are Periods and Epochs. Thus heavily cratered material in Noachis Terra defines the Noachian System position and the Noachian Period age category, and intercratered plains material defines

the Upper Noachian Series, corresponding to the Late Hesperian Epoch [1].

Increasingly, it is apparent that using material referents to define the spans of time-stratigraphic units on Mars does not work well, because of many uncertainties in the temporal character of the geologic units and the lack of temporal continuity among the referents. Also, photogeologic techniques necessarily limit the inspection of material units to surface exposure, and so little is known about their vertical character. Thus stratigraphic columns remain poorly defined. Some of the specific problems include: (1) The base of the Lower Noachian basement material is unexposed and thus remains stratigraphically undefined. (2) Middle Noachian cratered terrain and Upper Noachian intercrater plains materials are intergradational with each other as well as with older and younger units. This means that the ages of parts of the units fall outside the time-stratigraphic positions and periods they are meant to define. Also, the end of the Noachian is commonly viewed as when widespread valley formation and crater degradation largely ceased on Mars. However, some evidence indicates that that cessation may be time transgressive and controlled by elevation [10]. (3) Lower Hesperian ridged plains material is mapped in many areas across the planet, but some patches actually have Late Noachian crater densities [7]. Also, wrinkle ridges deform plains materials in caldera floors and northern plains surfaces, which reminds us that wrinkle ridges are not primary features and thus do not necessarily relate temporally to the materials they deform. Finally, MGS and MO data are revealing that Hesperian Planum itself may be complex stratigraphically. (4) Upper Hesperian complex plains material, representing the Vastitas Borealis Formation likely consists of sedimentary material related to inundation of the northern plains. The unit may represent a very brief moment in geologic time, rather than a truly expansive epoch. (5) The Lower and Middle Amazonian referents are deposits and lobate materials whose detailed histories remain to be determined. (6) The Upper Amazonian flood-plain material in Elysium Planitia now appears to be largely flood lavas that were emplaced in an extremely young and brief event.

Crater-Density Definitions and Precautions. Tanaka [1] used the type material referents to help determine the crater-density boundaries to the time-stratigraphic units, which has been a very useful application of that stratigraphic scheme. However, for stratigraphic applications, crater-density relative-age determinations have some serious limitations that need to be kept in mind. Crater densities provide, assuming no subsequent resurfacing, a mean surface age. Thus, unexposed, older parts of the unit cannot be accurately

dated, although in some cases the crater age of buried surfaces can be inferred by the density distribution of large, partly buried craters and depressions indicating possible buried craters. In addition, map units may include outcrops of greatly varying age, in which the crater sample size of individual outcrops may be insufficient to effectively constrain age. Thus, the standard deviation of the mean crater age may be a rather meaningless quantity when it comes to defining the age range of units. An extreme example would be a Hesperian crater density resulting from a map unit that includes individual outcrops of Noachian, Hesperian, and Amazonian material.

Another problem that is increasingly noted is the effects of resurfacing on crater counts. It has long been appreciated that degraded, ancient cratered surfaces on Mars have shown evidence of crater obliteration, both in surface morphology and crater distributions. Also, smaller craters appear to be obliterated at higher latitudes, which may relate to episodic growth and recession of ice-rich dust mantles until geologically recent time [11]. Even at equatorial latitudes, pedestal craters and formation of yardangs in materials including the Medusae Fossae Formation and layered deposits at Meridiani Planum indicate regional scale burial and exhumation. As a result, crater densities in many cases reflect exposure or retention ages that may be much younger than the emplacement age of the material units.

Recommendations for Updating the Formal Stratigraphic Scheme. As previously discussed, some of the referents for defining martian epochs are time transgressive across epoch boundaries, whereas others may represent only a small fraction of the epoch, as defined by crater counts. Because of the utility of crater-count boundaries and all the relative-age determinations that have been performed using the existing scheme, the best option may be to abandon the referent-based, time-stratigraphic approach that has been used, but continue to use the crater-density boundaries defining the epochs for the time being. Eventual updating of the scheme is still desirable, because until then, the association of the time-stratigraphic units with their referents will remain. A better scheme is the modified time-stratigraphic approach used for the Moon, in which significant impact and mare-emplacement events, dated by crater counts and radiometric ages of returned samples, are used as time-stratigraphic demarcations [12]. This scheme developed over time for, as in the case of Mars, rock units were inappropriately used to define time-stratigraphic units initially. To some degree, the lunar approach is bolstered by terrestrial work that appears to support the notion that some significant stratigraphic boundaries such as the Creta-

ceous/Tertiary may have resulted from impact or other short-lived events.

For Mars, significant widespread and notable events in the geologic record may include large impacts, huge volcanic eruptions, climate change as indicated by extensive high-latitude mantles and in the record of polar layered deposits, and emplacement of huge sedimentary deposits. A specific example is the expansive Vastitas Borealis Formation in the northern plains. This material appears to have been deposited in a geologically very brief span of time. As such, it could be used as an event referent marking the beginning of a "Borealian" Epoch or even Period. A general overhaul of the martian stratigraphic scheme, however, should await updated, systematic, planetwide geologic mapping based on the new MGS and MO data sets and improved mapping techniques discussed herein. (Any drastic changes in Mars stratigraphic nomenclature should be approved among a broad venue of martian mappers and crater counters for formal acceptance.)

Implications. A huge amount of work has already gone into geologic mapping and relative-age dating of Mars for the determination of local to global-scale geologic histories. Nevertheless, significant advances can and will come in how researchers formalize martian stratigraphy and in how well mappers interpret the geologic history of Mars, based on new data, improved techniques, and more thorough crater-density analyses. We recommend that new, planetwide systematic geologic mapping of Mars be undertaken. Moreover, obtaining the best results possible in reconstructing the geologic history of Mars with available data will be vital for intelligently targeting sites to meet the exploration objectives of future Mars missions.

References. [1] Tanaka K.L. (1986) JGR 91, E139. [2] Malin M.C. and Edgett K.S. (2001) JGR 106, 23,429. [3] Hansen V.L. (2000) EPSL 176, 527. [4] Salvador A., ed. (1994) International Stratigraphic Code. [5] North American Stratigraphic Code (1983) AAPG Bull. 67, 841. [6] Scott D.H. et al. (1986-87) USGS Maps I-1802-A,B,C. [7] Dohm et al. (2001) USGS Map I-2650. [8] USGS (1999) USGS Open-File Rep. 99-430. [9] Scott D.H. and Carr M.H. (1978) USGS Map I-1083. [10] Craddock R.A. and Maxwell T.A. (1993) JGR 98, 3453. [11] Soderblom L.A. et al. (1973) JGR 78, 4117. [12] Wilhelms D.E. (1987) USGS Prof. Pap. 1348.

IGNEOUS AND AQUEOUS PROCESSES ON MARS: EVIDENCE FROM MEASUREMENTS OF K AND Th BY THE MARS ODYSSEY GAMMA RAY SPECTROMETER. G. Jeffrey Taylor¹, W. Boynton², D. Hamara², K. Kerry², D. Janes², J. Keller², W. Feldman³, T. Prettyman³, R. Reedy⁴, J. Brückner⁵, H. Wänke⁵, L. Evans⁶, R. Starr⁷, S. Squyres⁸, S. Karunatillake⁸, O. Gasnault⁹ and Odyssey GRS Team. ¹Hawaii Inst. of Geophys. and Planetology, 1680 East-West Rd., Honolulu, HI 96822 (gitaylor@hawaii.edu). ²Lunar and Planetary Lab, Univ. of Arizona, Tucson. ³Los Alamos National Laboratory, Los Alamos, NM. ⁴Inst. of Meteoritics, Univ. of New Mexico, Albuquerque, NM. ⁵Max-Planck-Institut für Chemie, Mainz, Germany. ⁶Computer Sciences Corp., Lanham, MD. ⁷Dept. of Physics, Catholic Univ. of American, Washington, DC. ⁸Center for Radiophysics and Space Research, Cornell Univ., Ithaca, NY. ⁹Centre d'Etude Spatiale des Rayonnements, Toulouse, France

Summary: We report preliminary measurements of the concentrations of K and Th on Mars. Concentrations of K and Th and the K/Th ratio vary across the surface. Concentrations are higher than in Martian meteorites, suggesting that most of the crust formed by partial melting of enriched mantle. The average Th concentration (1.1 ppm), if applicable to the entire crust, implies a maximum thickness of about 65 km. The variation in the K/Th ratio suggests that aqueous processes have affected the chemistry of the surface.

Introduction: The concentrations of potassium and thorium on planetary surfaces reveal much of the story of crustal evolution. They are both incompatible elements, so they concentrate in magma. During igneous processing, the ratio of K to Th is approximately constant, so K/Th in igneous rocks reflects that ratio in the bulk silicate planet. However, aqueous processes can fractionate K from Th, in principle giving us a way to investigate the extent of aqueous alteration of a planetary surface.

Overview of Results: Data reduction techniques are described briefly in [1,2]. We present data from 45 S to 65 N only because high H concentrations at higher northern latitudes make corrections uncertain at present and because the data south of 45 S were obtained before boom deployment. K and Th are not uniformly distributed on Mars (Fig. 1-3). Some regions are richer in one or both of these elements than others. The northern plains from about 60 W to 180 E are rich in both, though the higher-than-average Th region extends much further south into the highlands. Both are generally medium to low over Tharsus, though there is a patch of higher K south of Olympus Mons. There is distinctly higher K and Th in Terra Sirenum in the region 30 to 45 S, 150 to 180 W, and in Terra Cimmeria (15 to 45 S, 150 to 189 E). The region west of Hellas contains average K, but has relatively high Th. The K/Th ratio varies widely. It is distinctly low west of Olympus Mons in Amazonis Planitia, in the region where Kasei Valles meets Chryse Planitia, in western Arabia Terra, and in Syrtis Major Planum. K/Th is high in the region surrounding and in Valles Marineris, Terra Cimmeria, and over much of Vastitas Borealis.

These variations probably reflect a combination of bulk Martian K and Th concentrations, igneous processes, and aqueous alteration. We hope to deconvolve these effects, and present preliminary interpretations below.

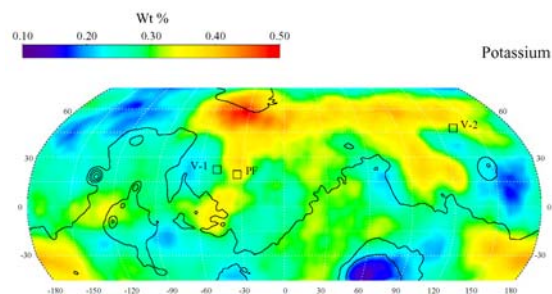


Fig. 1. K distribution on Mars. Data smoothed with 450 km boxcar filter.

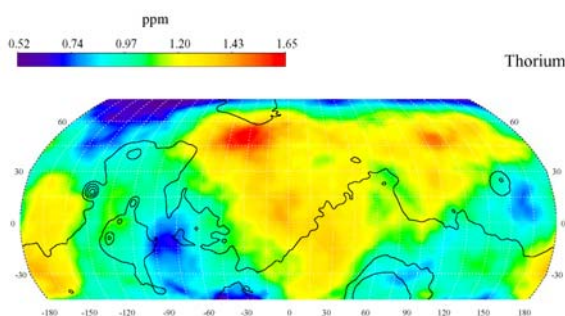


Fig. 2. Th distribution on Mars. Smoothed with 1200 km boxcar filter.

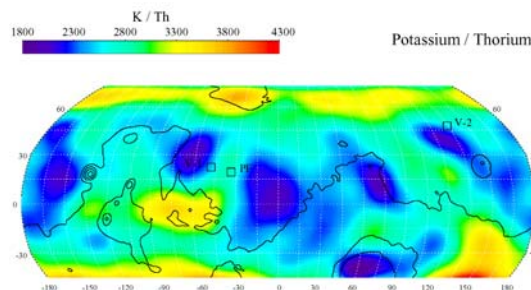


Fig. 3. K/Th varies significantly across Martian surface.

Bulk Martian Composition and Style of Primary Differentiation: K vs Th for the surfaces of Mars (unsmoothed 10-degree pixels) and the Moon (5-degree pixels[3]) is shown in Fig. 4. For a given Th content, the lunar surface contains much less K than does Mars. This reflects a large difference in K/Th in the bulk silicate portions of the two bodies, as we already knew from studies of SNC meteorites and lunar samples. The low lunar bulk K may reflect processes that operated during formation of the Moon by a giant impact [e.g., 4]. Martian meteorite data have been used to infer that Mars is enriched in moderately volatile elements such as K compared to Earth [5]. Because of the complexity of the surface, it is not yet possible to test the proposition that bulk silicate Mars has a higher K/Th than does the Earth. Nevertheless, the global data for K and Th are consistent with a somewhat higher K/Th for Mars, and Martian meteorite data clearly show that the Martian mantle was enriched in Mn and P, two other moderately volatile elements, compared to Earth [5,6].

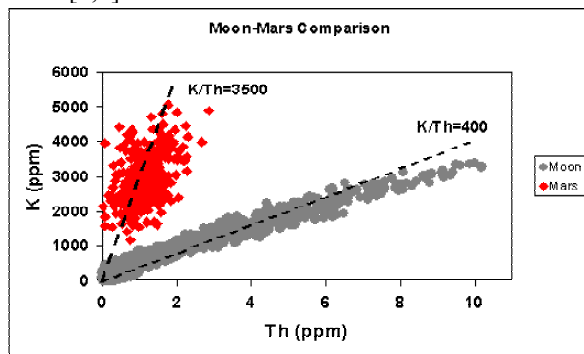


Fig. 4. K and Th variations on the lunar (5-degree pixels [3]) and Martian (10-degree pixels) surfaces. Dashed lines indicate constant K/Th ratios and are not fitted to the data.

The data in Fig. 4 can be used to probe the nature of the primary differentiation of Mars. The Moon has a much larger range in Th concentrations than does Mars. For the Moon this was caused by formation of a plagioclase-rich crust from a global magma system (called the magma ocean). Extensive fractional crystallization of the magma ocean also led to formation of materials enriched in Th and K (nicknamed KREEP). There is no evidence that extensive regions of exposed low-Th, low-K cumulates occur on Mars. Nor is there any evidence for the formation (or at least preservation) of extensively fractionalized products (the Martian equivalent of KREEP). This suggests that either a magma ocean did not form on Mars, that its characteristics (e.g., formation of garnet at its base, presence of water [7]) differed significantly from those of the lunar

magma ocean, or that its products are not exposed at the surface.

Crustal Evolution and Thickness: Global K and Th concentrations are generally higher than those in SNC meteorites (Fig. 5). Assuming the surface is representative of the entire crust, this suggests that the igneous rocks in most of the Martian crust are enriched compared to SNC basaltic meteorites in incompatible elements. This is consistent with models of Martian crustal evolution [8-12] that call on enriched and depleted reservoirs. The enriched component appears to have formed early in the history of Mars [10,11,13]. The high concentrations of K and Th in the Martian crust, especially if the crust formed early in Martian history, places constraints on the extent of melting after crust formation and the total heat production on Mars [14-15].

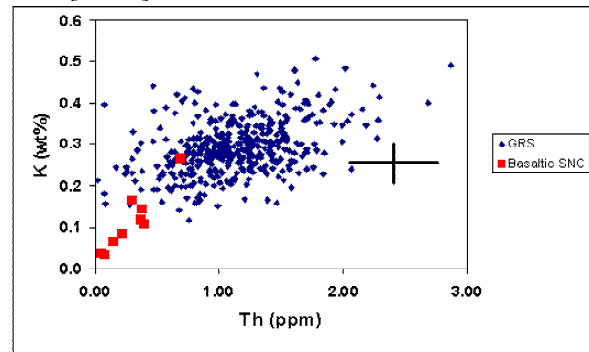


Fig. 5. K, Th variations on Mars compared to Martian (SNC) basaltic meteorites. Typical statistical uncertainty shown on right.

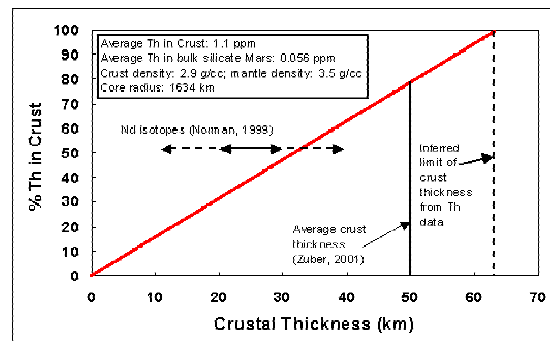


Fig. 6. Crustal Th vs. thickness of the crust.

We can use the average Th content of the surface to estimate the thickness of the crust (defined geochemically as the complement to the mantle). The average Th is 1.1 ppm. We assume that this surface average applies to the entire crust. Though not certain, there is no evidence to the contrary. Impacts early in Martian history churned over the highlands, producing a megaregolith that mixed the upper tens of kilometers

of the crust, as we suspect happened on the Moon. Dust and soils might represent at least a rough average of the upper crust. Finally, lava flows exposed on the surface might be similar in composition to magmas intruded at depth.

Assuming that this applies to the entire crust and that the primitive mantle had a Th concentration of 0.056 ppm [5], we find that 100% of the Th would be in a crust 65 km thick (Fig. 6). Since 100% partitioning of Th is unlikely, this is the maximum crustal thickness. If the average crustal thickness is 50 km [16], then the crust contains about 65% of the planet's bulk Th, in agreement with Norman's [8] estimate that 50-55% of the Nd is in the crust. This level of differentiation is not greatly different from that of the Earth.

K and Th as Monitors of Aqueous Alteration:

The K/Th ratio varies considerably on Mars (Fig. 3, 5). These elements behave reasonably coherently during igneous processing. Although they do vary somewhat among major groups of igneous rocks on Earth, their geochemical behavior during partial melting and fractional crystallization are very similar compared to their behavior during aqueous processing. We cannot rule out fractionation by igneous processes, especially at the extremes of fractionation [S. McLennan, personal communication]. K/Th varies among basaltic SNC meteorites (Fig. 5), though not to the extent it varies in our global data set. The Moon provides an excellent example of fractionation under extensive igneous processing, and the global data obtained by Lunar Prospector indicates that K/Th is relatively constant (Fig. 4). Thus, we are pursuing the idea that the variation in K/Th is caused at least in part by aqueous processes. We hope this ratio, and U data when counting statistics improve, will be a useful tool for studying aqueous processes on a global scale.

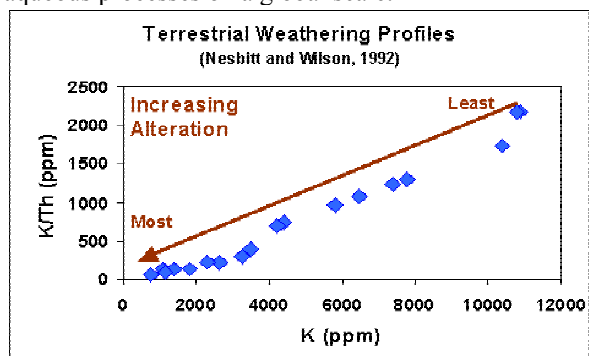


Fig. 7. Weathering of terrestrial basalt causes a depletion of K while Th remains constant, leading to reduction in the K/Th ratio.

Dissolution of K and Th depends on the solubility of the phases they are in: K in feldspar (plagioclase

and K-feldspar) and volcanic glass, and Th in phosphates, volcanic glass, and possibly in other accessory phases such as zircon and monazite. Experiments and measurements of weathering profiles illustrate the different behavior of K and Th. Nesbitt and Wilson [17] studied a terrestrial weathering profile in basalt (Fig. 7). Th is resistant to transport while K is very mobile. In this example, both K and Th were concentrated in residual glass in the lava flow studied.

Dreibus et al. [18; also Dreibus and Wanke, unpublished data] did leaching experiments on the Martian meteorites. They put pulverized meteorite powders in slightly acidic, saturated solutions of Mg_2SO_4 , and allowed the powders to be leached for minutes to hours. The results (Fig. 8) show that the REE and U were almost completely removed from the residue, while almost all of the K remained undissolved. They interpreted this to indicate that the leached elements were all contained in phosphates, while K was confined to plagioclase. This is another illustration that aqueous processes can fractionate K from U, and presumably from Th. (Th could not be measured by the INAA technique used, but would probably have behaved like U because it is contained in phosphates, too. Its behavior in the solutions might be very different from that of U, however.) Because P is abundant in SNC meteorites (and by inference in the Martian mantle), phosphate dissolution might be important in fractionating K from Th.

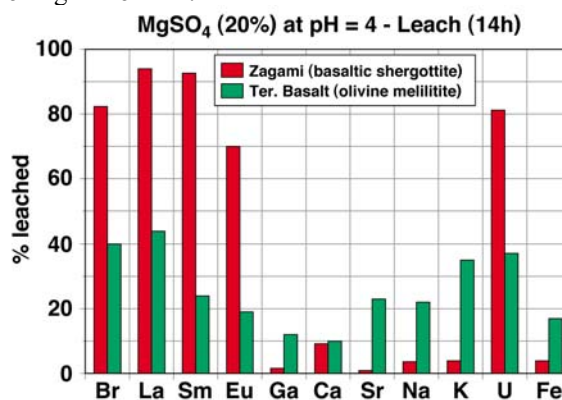


Fig. 8. Leaching experiments [18] on Martian meteorites show that mildly acidic solutions rapidly dissolve phosphate minerals, removing REE, U, and (presumably) Th from the residual solid. Terrestrial basalts may behave differently because of differences in siting of these trace elements.

Differential solubility of K-bearing phases and Th-bearing phases may have led to large-scale fractionation of K and Th, as shown in Fig. 3. The K/Th ratio and total abundances of each might serve as a monitor of global fractionation caused by aqueous processes

(weathering, hydrothermal alteration, fumerolic activity, etc.). However, to use this tool, we need more experiments and detailed geochemical modeling of trace element fractionation under Martian environmental conditions.

Conclusions: Although our data should still be considered preliminary, we can make some tentative conclusions: (1) The concentrations of K and Th and the K/Th ratio vary across the Martian surface. (2) The concentrations are significantly higher than those in SNC meteorites, suggesting different mantle sources for the meteorites compared to the bulk of the crust. (3) Most of the crustal igneous rocks could have formed from enriched mantle sources. (4) The concentration of Th on Mars does not vary as much as it does on the Moon, suggesting that the primary differentiation of Mars differed from that of the Moon. (5) If the average Th concentration of the surface is equal to the average of the entire crust, the crust cannot be thicker than 65 km. (6) The mean Th concentration is consistent with a crust 10s of km thick. (7) Aqueous processes have played an important role in the fractionation of K from Th.

Acknowledgments: We thank all members of the GRS team for instrument, data reduction, and computer support. This work is supported by NASA.

References: [1] Boynton, W. B., et al. (2003) *LPS XXXVI*, Abstract #2108. [2] Reedy, R. et al. (2003) *LPS XXXIV*, 1592. [3] Prettyman, T. H, et al. (2002) *LPS XXXIII*, Abstract #2012. [4] Drake, M. J. and Righter, K. (2002) *Nature* **416**, 39-44. [5] Wänke, H. and Dreibus, G. (1988) *Phil. Trans. R. Soc. Lond. A* **325**, 545-557. [6] Halliday, A. et al. (2001) *Space Sci. Rev.* **96**, 197-230. [7] Hess, P.C. and Parmenier, E. M. (2001) *LPS XXXII*, Abstract #1319. [8] Norman, M. D. (1999) *MAPS* **34**, 439-449. [9] Norman, M. D. (2002) *LPS XXXIII*, Abstract #1175. [10] Borg, L. et al. (1997) *Geochem. Cosmochem. Acta* **61**, 4915-4931. [11] Wänke, H. et al. (2001) *Space Sci. Rev.* **96**, 317-330. [12] McLennon, S. (2002) *LPS XXXIII*, Abstract #1280; also submitted manuscript. [13] Halliday, A. et al. (2001) *Space Sci. Rev.* **96**, 197-230. [14] McLennan, S. (2001) *Geophys. Res. Lett.* **28**, 4019-4022. [15] Hauck, S. and Phillips, R. J. (2002) *J. Geophys. Res.* **107**, 10.1029/2001JE001801. [16] Zuber, M. T. (2001) *Nature* **412**, 220-227. [17] Nesbitt, H. W. and Wilson, R. E. (1992) *Am. J. Sci.* **292**, 740-777. [18] Dreibus, G. et al. (1996) *LPS XXVII*, 323-324.

THE MICROSCOPE FOR THE BEAGLE 2 LANDER ON ESA'S MARS EXPRESS. N. Thomas^{1,2}, S.F. Hviid¹, H.U. Keller¹, W.J. Markiewicz¹, T. Blümchen¹, A.T. Basilevsky^{1,3}, P.H. Smith⁴, R. Tanner⁴, C. Oquest⁴, R. Reynolds⁴, J.-L. Josset⁵, S. Beauvivre⁵, B. Hofmann⁶, P. Rüffer⁷, C.T. Pillinger⁸, M.R. Sims⁹, D. Pullan⁹, and S. Whitehead⁹

¹Max-Planck-Institut für Aeronomie, Max-Planck-Str. 2, D-37191 Katlenburg-Lindau, Germany, ²Physikalisches Institut, University of Bern, Sidlerstr. 5, CH-3012 Bern, Switzerland, ³Vernadsky Institut, Moscow, Russia, ⁴Lunar and Planetary Lab. University of Arizona Tucson, Arizona, U.S.A., ⁵Micro-Cameras & Space Exploration (SPACE-X), Neuchatel, Switzerland, ⁶Natural History Museum, Bern, Switzerland, ⁷Institut für Datentechnik und Kommunikationsnetze der TU Braunschweig, Braunschweig, Germany, ⁸Dept. of Earth and Planetary Sciences, Open University, Milton Keynes, U.K., ⁹Dept. of Physics and Astronomy, University of Leicester, Leicester, UK.

Introduction: The European Space Agency (ESA) will launch the Mars Express spacecraft in June 2003. The mission is intended to provide a flight opportunity for re-builds of experiments lost as a result of the Russian Mars '96 launch failure and will reach Mars around Christmas 2003. The re-build has allowed several instruments to be improved and upgraded. However, a completely novel element of the Mars Express payload is the Beagle 2 lander.

Beagle 2 is designed to descend through the atmosphere of Mars to the surface using a combination of aerobraking, parachutes, and airbags. After coming to rest in the Isidis Planitia region of Mars, (260-270°W, 5-10°N), the lander will deploy solar panels and begin scientific operations. The scientific payload comprises an X-ray fluorescence spectrometer, a Mössbauer spectrometer, a stereo camera system, a stepped combustion mass spectrometer (GAP), a sampling device ("PLUTO"), a set of environmental sensors, and a microscope.

Most of the experiments (the exceptions being the GAP and the environmental sensors) are mounted on a robotic arm referred to here as the ARM. The end of the ARM has a flat experiment "platform", referred to as the PAW (position adjustable workbench), on which the experiments are mounted.

In addition to the experiments, a grinding and coring tool is also available on the PAW to scratch and flatten the surfaces of rocks within reach of the ARM.

This paper describes the aims and performance of the microscope on the Beagle 2 PAW.

Scientific Objectives: A microscope has four distinctly different tasks in a lander package. Firstly, the instrument can be used to study the physical and structural properties of a surface and hence make a geophysical analysis and contribute to the overall geological and mineralogical interpretation of the landing site.

Secondly, a microscope can contribute to studies of the atmosphere of Mars. Specifically, dust particles are

continuously precipitating out of the dusty atmosphere and hence a microscope can be used to constrain the sizes and shapes of particles for input into atmospheric scattering and radiative transfer models of the Martian atmosphere.

Thirdly, the instrument can be used to characterize and/or select a sample before it is passed to another analytical instrument. It is used therefore to assist the chemical analysis.

Finally, the instrument can be used to study the morphology of a potentially biological sample and hence identify structures which are characteristic of past or present biological activity.

Instrument Concept: The concept of the optics for the microscope was based on a system originally designed for the Mars Environmental Compatibility Assessment (MECA) experiment package which was slated for launch on the cancelled Mars '01 mission.

The detailed design of the microscope for Beagle 2 was constrained by even more stringent mass and volume limits. This suggested that we try to keep the focal length of the experiment as short as possible. This, in turn, implied that we should select a relative short working distance (the distance between the object position and the first optical element) of the order of 12 mm. This was considered a reasonable solution given that the ARM would be able to bring the microscope to the sample. The optically active elements comprise a Cook triplet. The optics provides a magnification of 3.5:1.

The sample is unlikely to be well illuminated by sunlight because the microscope itself shadows the sample. This implied that an illumination system would be required. Microscopes in the laboratory use either transmissive illumination or confocal illumination. While a confocal system is desirable, at present the development of such a method of illumination for spaceflight is only at a preliminary stage. For Beagle 2,

we have chosen to use light-emitting diodes (LEDs) mounted around the entrance aperture of the microscope. The system comprises 12 LEDs, 3 red, 3 green, 3 blue and 3 UV. The UV LEDs are designed to induce fluorescence in rocks (or a biological sample). A filter has been introduced into the optics to eliminate reflected UV from the incoming beam.

For mass reasons, it was decided to use a micro-camera head including a CCD detector and its associated electronics (detector control electronics, analogue to digital converter, noise reduction filters, clock, memory buffer, serial digital interface drivers, and 10 Mbit s⁻¹ communication protocol) in a lightweight (ca. 80 g) highly integrated 3D module. This micro-camera has benefited from developments by SPACE-X within a contract from the ESA Technical Research Programme (TRP). The 14 micron pixel pitch leads to a pixel scale of 4 micron px⁻¹. The CCD is a 1k

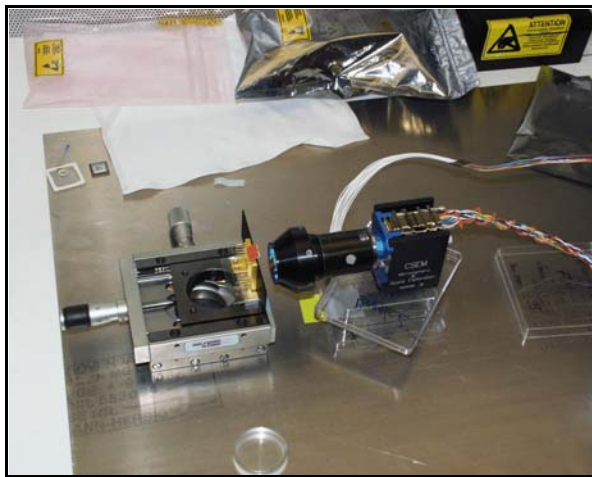


Figure 1 The FM microscope views a target mounted on a translation stage during bench testing.

x 1k device giving a field of view of just over 4 x 4 mm².

Even before detailed design commenced it was clear that the depth of focus of the microscope would be under 100 microns. It was also apparent that the accuracy with which the PAW could bring the microscope to the sample would be at least a factor of 20 larger than this. Thus, a focussing mechanism was necessary. Translation of the entire microscope at the interface to the PAW was implemented. The PAW provides a means of bringing the microscope to within ± 3 mm of its target. A "thumb" on the PAW prevents the microscope from impacting

rocks unless their surface roughness is greater than ± 12 mm (the working distance). The full range of the stepper motor is ± 3 mm, matching the accuracy of the PAW motion. The instrument is shown in Fig. 1.

Test Results: An image scale of 4.075 micron px⁻¹ at the best focus position was derived in bench tests. The variation in the image scale across the field of view of the microscope corresponds to a 0.2% distortion. The FWHM of a point source at the nominal focus position is 4.50 microns (1.10 px) and is less than 6 microns (1.5 px) within 50 microns of the nominal focus position. This result indicates that the accuracy of the stepper motor motion (20 microns) should be more than sufficient.

The flat-field shows some slight evidence of vignetting at the corners of the FOV. This is partly due to a slight misalignment of the detector in its housing and partly due to the baffling system.

The red LEDs are slightly susceptible to temperature and their central wavelength decreases from nominal (642 nm) at room temperature to 625 nm at 183 K. The wavelengths of the other LEDs vary by less than 2 nm over this temperature range. The output of the UV LEDs is strongly temperature dependent below 220 K and they become very faint below 200 K.

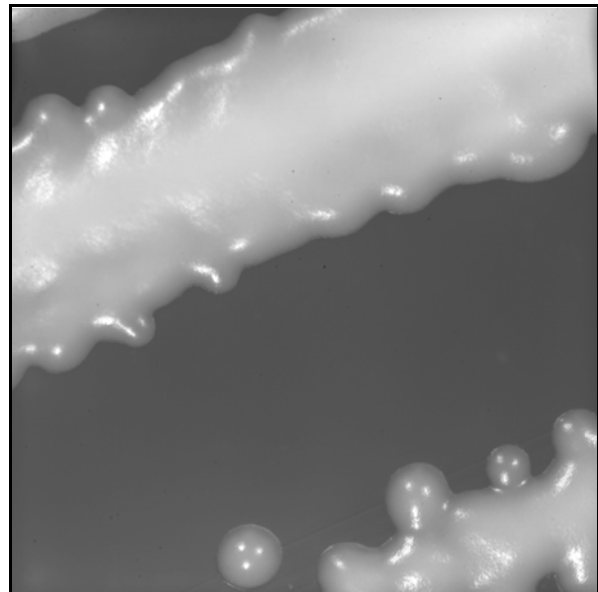


Figure 2 Microscope image of yeast on agar. The field of view is 4 x 4 mm². The bright dots on the surface of the yeast come from specular reflections from the LEDs. Individual organisms are below the resolution limit.

The illumination field has been calibrated for all LED combinations and the system absolute response computed. (Care needs to be taken here because, unlike most imagers, the microscope also provides the irradiance of the target.)

For amusement we show in Figure 2 an image of some yeast grown on agar. This shows that the microscope still does not have high enough resolution to resolve individual organisms.

Flight Software: The microscope can generate a huge volume of data. In particular, because we have no a priori knowledge of the focus position and because different parts of the field will have different focus positions as a result of surface roughness, many images at different positions need to be acquired to ensure that all parts of the field are in focus at some point. Potentially, 60 or more images may be required to guarantee that we obtain all parts of the field in focus at some stage.

Two approaches to solving the problem of data volume have been implemented on Beagle 2. Firstly, a wavelet compression algorithm has been incorporated into the lander software to reduce the total data volume from the experiment. The algorithm will also be used to support the other imaging experiment (the stereo panoramic camera) onboard Beagle 2. Wavelet compressors resolve the image into a series of coefficients which are related to spatial frequencies. The more detail one wishes to see in an image, the more coefficients one has to return. For the microscope this scheme is extremely effective. The reason is because an out of focus image does not require many coefficients. It is smooth. Therefore, unfocussed frames compress extremely well with ratios in excess of 40:1 often achievable with almost no loss. Hence, one possibility is to transmit all 60 frames compressed according to a quality criterion.

The second approach is to analyse the data onboard. Here we acquire all 60 frames but investigate the entropy at each position in each image to determine which image has the best focus for that position. We then downlink a completely focussed composite image.

In both cases, an important result from the analysis is that the image in which focus has been achieved for a position allows us to define unambiguously its depth. Hence, not merely does the microscope give us a 2-D picture of the surface, it also gives us a depth map allowing complete 3-D reconstruction of the surface.

Summary: The microscope for Beagle 2 is a highly compacted (160 g) device which will provide 6 micron resolution images of surface material in Isidis Planitia. The elegant design of the system makes it ideal for future landed missions where microscopic imaging might be required. Adaptation of the system to support other experiments (e.g. Raman spectrometer or laser mass spectrometer) should be relatively straightforward.

This abstract is a summary of a more detailed instrument paper submitted to Planetary and Space Science.

Acknowledgments: The development of the microscope optics was funded by the University of Arizona's special fund. The micro-camera head was sponsored by SPACE-X. The Max-Planck-Gesellschaft supported integration and test. Software development was partly sponsored by DLR. The Beagle 2 PAW microscope focussing mechanism was funded by the Particle Physics and Astronomy Research Council of the UK. M.R. Sims acknowledges funding from the University of Leicester and via the Royal Society Industry Fellow scheme.

THE SOUTH POLAR RESIDUAL CAP OF MARS: LANDFORMS AND STRATIGRAPHY. P. C. Thomas¹

¹Center for Radiophysics and Space Research, Cornell University, Ithaca NY, 14853.

The south polar residual cap (sprc) of Mars is morphologically distinct from that in the north, and is largely compositionally distinct as well, apparently dominated by CO₂ rather than the H₂O present in the northern residual cap. This work addresses questions of the history and significance of these distinctive deposits by mapping the many forms using MOC images and MOLA data.

Depositional units: There are two primary sets of depositional units in the sprc: 1) An older unit, approximately 11 m in thickness with four included layers, widely distributed over the sprc, and expressed as mesas or broad surfaces cut by a variety of circular to linear depressions, and commonly having polygonal troughs (Fig. 1a).

2) One or more younger units, approximately 2 m thick, that have superposed and filled depressions formed in the older unit, and also formed in local discrete deposits. This unit also has a wide variety of depression types (Fig. 1b, c) Both of these sets of units occur on the flatter topography of the polar deposits (slopes under 2°), and terminate in troughs at elevations only a few m lower than where the layers are fully developed. Both units show scarp retreat of up to a few m over one Martian year [1].

Erosion and other modification forms: The sprc topography has unique erosional topography [2,3]. There are a great variety of these forms, many are seen to merge into other forms. While the large circular depressions have received the most attention, these are not even the “typical” form. We have mapped the following forms: generic depressions, large circular depressions, parallel sets of linear depressions (fingerprint terrain), other linear depressions, moats, and curled depressions, among others

Fingerprint depressions define a few coherent patterns, and are not simply oriented with one side toward the pole; their consistent trends suggest underlying structural control; their shapes show common upper surface fracture control (Fig. 1e). They occur in a restricted area of the sprc (Fig. 2a).

The *curl* depressions (Fig. 1d,f) are oriented with openings dominantly within 60° of north (Fig. 2d). The surface indenting the curl commonly is in a ramp form (Fig. 1f), rather than a pedestal.

Moat-like depressions occur within some nearly circular forms as well as bounding a variety of mesas and other remnant topography. Moats within other depressions show two distinct widths: ~20 m and ~70 m. The latter is indistinguishable from moat widths around mesas and other remnants (Fig. 2c).

Development of the depressions and deposits: Changes between 1999 and 2001 indicate some backwasting of the forms of order 1-4 m/ Mars year [1], with a few instances over 5 m. Initiation of the forms, and enlargement of many, however, involve mechanisms other than backwasting of steep scarps. Disruption of the older upper surface occurs at least in part by sag and collapse; development sequences of curled depressions can be found, and examples of enlargement almost entirely by collapse are also found (Fig. 1d,i). The sag and collapse features may explain the de-

velopment of “escher” terrain, whereby an upper surface appears contiguous between different cycles of erosion (Fig. 1j).

Thin layers preferentially develop pits and other depressions over underlying topography, and on some upper convex slopes (Fig. 1b). These pits, “peels”, and moats indicate modification of overlying deposits by exposure of relief or a critical layer thickness. There are examples of inverted relief, wherein the older, thick deposits have collapsed after deposition of thin deposits within the large depressions .

Non-uniform deposition is also found in some tongues of material several m in depth and a few hundred m long in restricted areas of the sprc. These appear to be part of the later deposits.

Pattered ground: Slopes from remnants of the thick, older unit commonly show surfaces with brick or cobblestone appearance, sometimes giving a false impression of large numbers of layers exposed in the mesas (1a). Material underlying the sprc in some troughs displays a slightly different patterned appearance.

Interpretations: Several different cycles/changes in polar depositional and sublimational regime are indicated:

- 1) Change from main polar layered deposits to deposition of the 11 m set of layers: H₂O rich deposits to CO₂ rich ones.
 - 2) Cycles producing layering within the 11 m stack, about 4 cycles. Some differences in physical characteristics/ composition.
 - 3) Significant erosion of the deposits in the form of merging depressions and sag and collapse modification.
 - 4) Before or during the subsequent steps, development of polygonal troughs in much of the surface of the thick deposit.
 - 5) Deposition of one or two, ~ 2 m layers in the erosional topography of the thick deposits.
 - 6) Renewed sublimation of both deposits. Included in this step is the scattered development of inverted relief. This activity may continue at present.
- The primary interpretive difficulty is the similarity and merging of deposits formed by sag and collapse of the thick units, and thinner, younger layers (step 5 above). Both units are clearly present; however, which is present at a particular site is sometimes unclear.
- The evident variety of layer types, thicknesses, and cycles of deposition and erosion (including inverted relief) show there are several combinations of composition and/or texture within these deposits. More than one type of climate cycle is required to form these features’ current appearance.

References:

- [1] Malin, M. C., M. A. Caplinger, and S. D. Davis (2001). *Science*, 294, 2146-2148. [2] Thomas, P. C. et al. (2000). *Nature* 404, 161-164. [3] Byrne, S., and A. P. Ingersoll (2003). *Science* 299, 1051-1053.

Acknowledgements: Help was provided by Mike Malin, Ken Edgett, Scott Davis, Bruce Cantor, Rob Sullivan, and Lisa Wei.

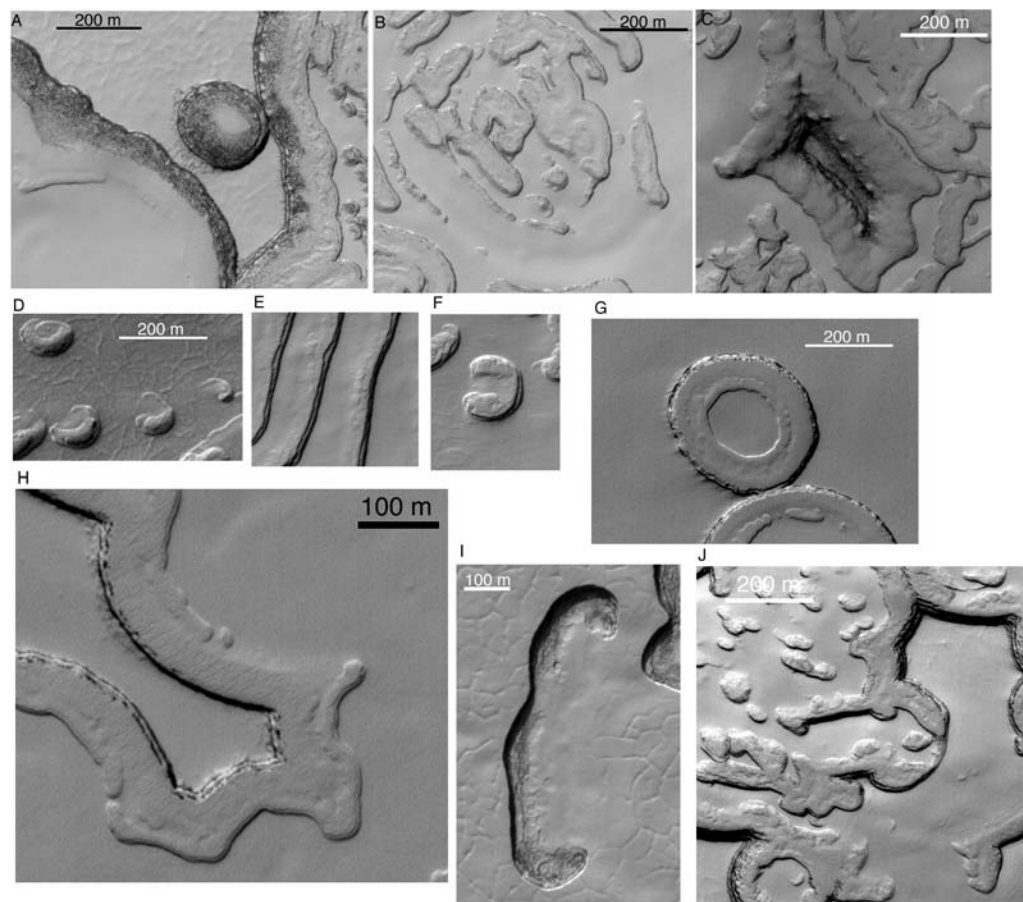


Figure 1a. Surface of thicker sprc unit, with polygonal troughs and darker patterned materials flanking slopes of 3-4 layers. Moat to the right. b). Erosion of thinner layers in places follows underlying topography, here part of a curving ridge in the lower left. Sun from lower right. c. Thinner unit eroded in moat from underlying topography. d. Depressions with fracture boundaries showing development sequence toward a curl depression. e. Fingerprint trough. f. Curl trough, showing interior ramp. g. Confined moats. h. Moat, showing textured lower surface, probably the main polar layered deposits. i. Linear depression and sag. j. "Escher" terrain with uncertain relation of upper and lower surfaces, probably generated in part by sag and collapse as in Fig. 1 i.

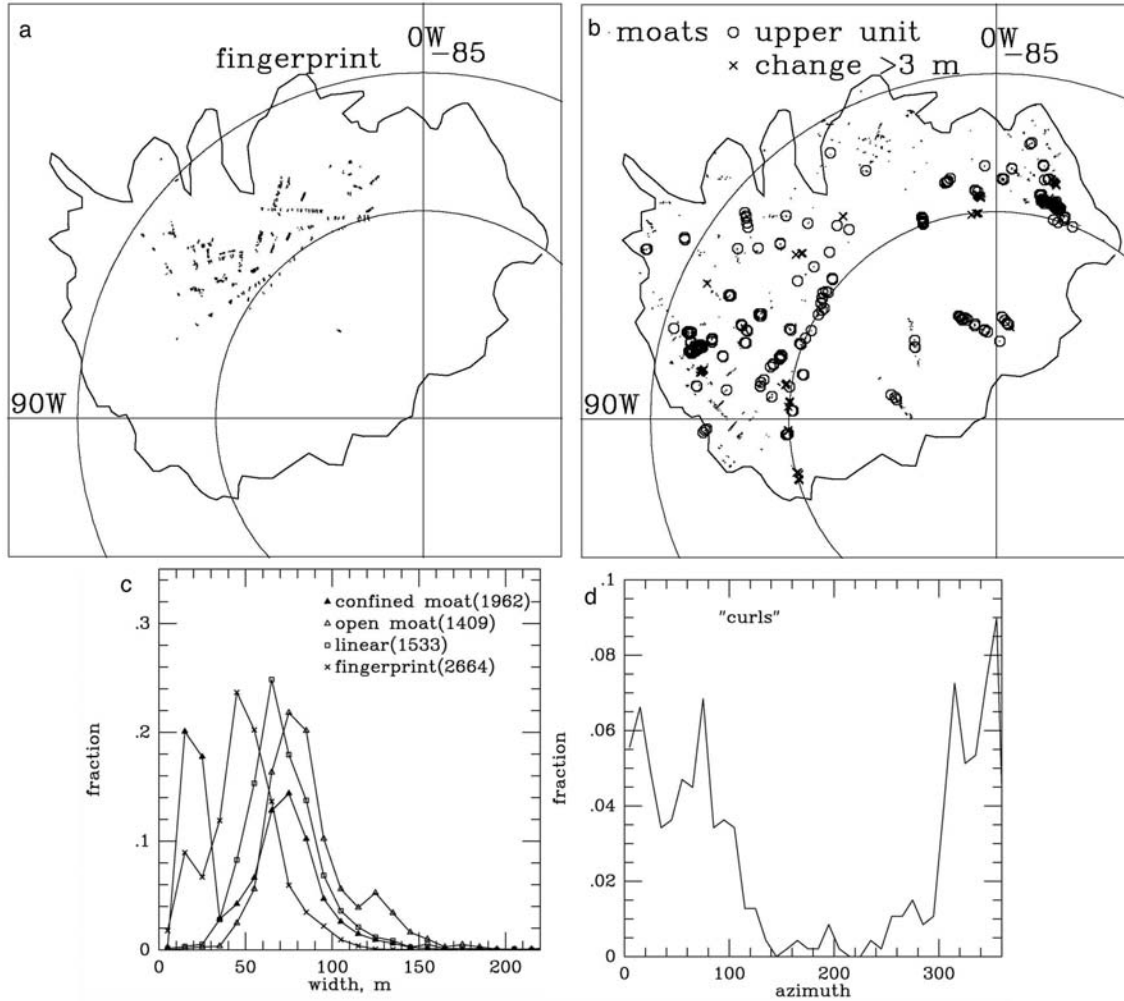


Figure 2. Some characteristics of the south polar residual cap erosional forms. a) Location of fingerprint terrain. b) Locations of upper surface of thick unit (circles), and most kinds of moats (small dots). Both forms are widespread over the sprc. Locations of changes measured in excess of 3 m in one Mars year shown by x's (Measured change is 6 m or more across walls or depressions; single distance is 3 m or more.) c) Widths of some depression types. Note the similarity of open and confined moats and linear depressions; slight distinction of the fingerprint depressions. d) Orientation, clockwise from north, of the curl depressions. The orientation would be to the left in Fig. 1f.

CARBONATES ON MARS: PROBABLE OCCURRENCES, SPECTRAL SIGNATURES, AND EXPLORATION STRATEGIES. B. J. Thomson and P. H. Schultz, ¹Brown University, Department of Geological Sciences, Box 1846, Providence, RI 02912 (Bradley_Thomson@brown.edu).

Synopsis: Carbonates and other aqueous alteration products occur in the SNC meteorites [1,2], and spectral observations suggest that carbonate is present in Martian dust as a minor constituent [e.g., 3-7]. Analysis of analogous terrestrial dust deposits (loess) in Argentina, which also contain a significant carbonate component, has revealed that post-depositional modification of the loess can result in the reprecipitation of carbonate as concretions and as discrete layers of calcrete. These Argentine deposits give us a roadmap for locating the most accessible carbonate deposits on Mars.

Introduction and background: The presence of carbonates on Mars has long been surmised as a sink for CO₂ on the basis theoretical models of the evolution of the Martian atmosphere [8,9]. The character, abundance, and distribution of carbonates are important parameters for assessing the paleoclimate and volatile evolution of Mars.

Carbonates have been tentatively identified with spatially coarse telescopic spectral studies [e.g., 2-6]. With higher spatial resolution data of TES, regional outcrops (>10km²) of moderately-grained carbonate-rich material were not detected, despite a thorough search [8]. However, recent analyses of the carbonate absorption feature near ~7μm in TES data has identified fine-grained carbonates at the ~2-3wt% level in Martian dust [7].

The dust appears to have been globally homogenized and is decoupled from the underlying surface. The distributed carbonate component in the dust is likely derived from the weathering of more concentrated sources. A lack of regional carbonate-rich outcrops may indicate that primary carbonate deposits are either mantled or deeply buried.

Additional information about the ultimate fate of carbonates is provided by the SNC meteorites, of which all subgroups contain traces of water-deposited minerals [1]. The formation ages of these secondary mineral assemblages tell us about the timing of fluid flux through the upper crust of Mars. Radiometric ages of the carbonates range from ~4 Ga to ~0.7 Ga in ALH84001 and Nakhla, respectively [9,10]. Coupled with the lack of extensive alteration of the silicate phases, this indicates that the responsible fluids did not spend a long time in contact with these rocks but were intermittently active over the bulk of Martian history. The upper crust of Mars may have experienced epi-

sodic “wetting events” that leached and reprecipitated carbonates in the subsurface.

Carbonates in loess. We propose that the post-depositional evolution of carbonates in Martian dust may be similar to the evolution of carbonates in Argentine loess deposits. Carbonates are present in two forms in the loess: they are found as fine-grained distributed components and are also concentrated into concretions or calcrete layers (Figure 1). The carbonate fraction of typical Argentine loess varies between about 2-4% [11].

Accumulations of carbonate, locally known as *toscas*, are widely distributed throughout Argentine loess sequences [12]. Formed through the downward leaching and reprecipitation of soluble components into lower soil horizons, these illuvial calcretes develop *in situ* and may cement and/or replace the host material. The calcrete morphology can be highly variable depending on the degree of development and local structural control. Observed forms include concretions or nodules, reticular and string-like patterns, and layers or hardpans (see Figures 1,2) [12]. These carbonates can generally be classified as pedogenic calcretes [13], although some sections may contain additional carbonates derived from laterally moving groundwater (which is not strictly a pedogenic process). The salient point is that carbonates are a mobile component in the subsurface that commonly form local concentrations of calcrete.

Spectral detection of carbonates: The planer carboxyl (CO₃²⁻) ion has six fundamental vibrational modes, of which two are degenerate and one is infrared inactive [e.g., 14,15]. The exact shape and position of vibrational absorption bands varies with the cation species: e.g., calcite (Ca), dolomite (Ca,Mg), magnesite (Mg), and siderite (Fe). The strongest infrared absorption features in calcite occur at 7.0 μm (asymmetric stretch), 11.4 μm (out-of-plane bend), and 14.0 μm (in-plane band) [15]. Additional combination and overtone features are present in the near infrared.

Detecting carbonate absorption features in field exposures of carbonates can be difficult due to the loss of spectral contrast from surface roughness at a variety of scales [16]. This includes roughness at the outcrop scale between individual boulders and cobbles, rough surface textures on exposed blocks, and microscopic roughness [17]. We are in the process of documenting the spectral signature of calcrete layers exposed in

section in loess deposits in the visible, near-infrared, and thermal infrared regions to assess the detectability of these deposits with rover-mounted instrumentation.

Exploration strategies: The most readily accessible concentrations of carbonates on Mars are likely reprecipitated calcrete layers within dust deposits. The potential for entombment and preservation of organic material in chemical precipitates makes these layers a high-priority target for exobiology [18]. Depending on the degree of cementation, these calcretes may form resistant hardpans that are exposed through differential erosion. However, due to mantling by continued dust deposition, exposed calcrete horizons may be difficult to spectrally detect. In addition, terrestrial calcrete hardpans are known to weather to boulders, cobbles, and smaller fragments [19] that will increase macroscopic roughness and reduce spectral contrast, thus further complicating spectral detection.

Perhaps a more likely locale where an unambiguous spectral signal may be obtained is in high slope areas where the subsurface profile is exposed (i.e. cliffs, mesa edges, channel walls). Calcrete layers tend to form steeply inclined surfaces in vertical exposures due to their high mechanical strength and thus may be relatively dust-free and clear of fragmental material. They may be more readily identifiable with visible/near-infrared imaging Pancam and thermal infrared spectrometer Mini-TES on the 2003 Mars Exploration Rovers than from orbital imaging/spectral platforms.

Another potential target of interest for sample-return missions is impact glasses derived from carbonate-bearing lithologies. Chemical systematics in impact glasses of various ages could provide a record of the isotopic evolution of the Martian atmosphere [20].

References: [1] Gooding J. L. (1992) *Icarus*, 99, 28-41. [2] Bridges J. C. et al. (2001) *Space Sci. Rev.*, 96, 365-392. [3] Blaney D. L. and McCord T. B. (1989) *JGR*, 94, 10,159-10,166. [4] Pollack J. B. et al. (1990) *JGR*, 95, 14,595-14,627. [5] Calvin W. M. et al. (1994) *JGR*, 99, 14,659-14,675. [6] Lellouch E. et al. (2000) *Planet. & Space Sci.*, 48, 1393-1405. [7] Bandfield J. L. et al. (2003) *LPS XXXIV*, abstract #1723. [8] Christensen P. R. et al. (2001) *JGR*, 106, 23,823-23,871. [9] Borg L. E. et al. (1999) *Science*, 286, 90-94. [10] Swindle T. D. (2000) *Met. Planet. Sci.*, 35, 107-115. [11] Teruggi M. E. (1957) *J. Sed. Petrol.*, 27, 322-332. [12] Zarate M. A. and Fasano J. L. (1989) *Palaeoeco., Palaeoclim., Palaeoeco.*, 72, 27-52. [13] Goudie A. S. (1983) in *Chemical Sediments and Geomorph.*, Academic Press, 93-131. [14] Clark R. N. (1999) in *Remote Sensing for the Earth Sciences*, John Wiley & Sons Inc., 3-58. [15] van der Marel H.

W. (1976) *Atlas of Infrared Spectroscopy of Clay Minerals and their Admixtures*, Elsevier Sci. Pub. Co., 396 pp. [16] Kirkland L. et al. (2002) *Remote Sens. Env.*, 80, 447-459. [17] Kirland L.E. et al. (2002) *Proc. SPIE*, 4495, 158-169. [18] Farmer J. D. and Des Marais D. J. (1999) *JGR*, 104, 26,977-26,995. [19] Netterberg F. and Caiger J. H. (1983) in *Residual Deposits*, Blackwell Sci. Pubs., 235-243. [20] Delano J. W. (1988) *LPI Tech. Rpt.* 88-07, 63-64.



Figure 1. Sea-cliff exposure of loess in Argentina showing single well-developed calcrete layer.



Figure 2. Exposure of loess sequence in Argentina showing more complex morphology of calcrete deposits.

GREAT MARTIAN DUST STORM PRECURSOR? J. E. Tillman, *Department of Atmospheric Sciences, University of Washington, Seattle, WA, USA (mars@atmos.washington.edu)*.

Reviews of rejected proposals for analyses of Viking lander meteorology data sometimes have stated that nothing significant remains to be learned: it is proposed that lander temperature differences between the first and second year prior to the dust storm season, may be related to or even be used as a predictor of whether or not great dust storms form later in the year. The Viking lander mission demonstrated conclusively that some years have great dust storms while others do not, contrary to conventional wisdom prior to the Viking results which suggested that they occurred every year. The first year had two, beginning at about L_s 210 (1977 A) and 310 (1977 B), the second and third had none, while the fourth year had one that was initiated about L_s 200 (1982).

Atmospheric temperature data were processed and averaged into 25 segments/sol, i.e., roughly hourly averages for almost all of the Lander 2 but far less than half of the Lander 1 mission. (The Lander 1 data were only partially processed due to problems with the wind determination.) From these, the minimum, sol average and maximum temperatures were determined for each sol. Lander 2 temperatures between roughly L_s 117 and 177, prior to the beginning of the great dust storm season, show that the minimum and daily average temperatures were essentially identical for the first year, with, and the second year, without, great dust storms, while the maximum temperature for the first year was consistently lower on a sol by sol basis by 3 to 9 degrees Celsius. This implies that the first year was dustier than the second and poses the question "Do these temperature differences truly indicate optical depth changes, and thereby atmospheric heating changes, and if so are these responsible for the presence or absence of great dust storms later in a given year?" Alternatively, are they artifacts or not significantly material to the circulation later in the year. The Lander 2 evidence for this possible dust storm precursor

condition will be presented.

Unprocessed Lander 1 data exist that can support or refute this hypothesis for most of this same season during years 1 and 2, a small portion of year 3, and for the first part of year 4 prior to its great dust storm. Lander 1 data have been processed for this season only in year 1, due to problems with the wind sensors that do not directly affect the temperature observations. (These wind sensor partial failures occurred in the first year, the first at L_s 117 and the second at L_s 303.) These unprocessed Lander 1 temperature data should be processed and analyzed to support, refute or modify this hypothesis and be compared with other data related to optical depth such as the second harmonic of the daily pressure variation which is a very good optical depth proxy. If these additional data are consistent with this hypothesis, then they must be modeled to see if such temperature observations are great dust storm precursors and thereby can be used to forecast great dust storms later in the same year. This potential illustrates why it is essential to reinstate climate observations as soon as possible, beginning at the Viking sites, and to make them permanent.

The Viking data are the only climate data for the surface of Mars and will remain so for the foreseeable future. It is now possible to far better process and analyze the Lander 1 wind data due to the dramatic improvement of computer resources since these efforts were terminated. Processing is still possible since all of the software, documentation and data have been maintained, without support, during the past decade and illustrations of the additions to this surface meteorology climate record will be presented. It is essential that an international program be immediately initiated to understand, replicate, further process, and improve the Viking Lander meteorology climate record, the only one for Mars, before this opportunity is permanently lost.

TEMPORAL AND SPATIAL DISTRIBUTION OF SEASONAL CO₂ SNOW AND ICE. T. N. Titus¹ and H. Kieffer¹, ¹ U.S. Geological Survey, 2255 North Gemini Dr., Flagstaff, AZ 86001.

Introduction: The seasonal polar caps are a major element of Mars' climate and global atmospheric circulation. Theoretical calculations [1,2] and surface pressure measurements [3] indicate that about ¼ of the CO₂ in the atmosphere condenses each year to form the seasonal caps. Changes in the polar cap albedo or emissivity modify the polar cap energy budget and the amount of CO₂ condensation, consequently affecting the global martian climate.

Variations in both albedo and emissivity have been observed by several spacecraft. In the 1970s, spacecraft observations of the polar regions of Mars revealed polar brightness temperatures that were significantly below the expected kinetic temperatures (140 - 148 K) for CO₂ in sublimation equilibrium with the martian atmosphere [4]. The observational footprints were typically a few hundred kilometers in diameter, with 20 μm brightness temperatures (T₂₀) as low as 130 K and had characteristic durations of a few days [4]. For historical reasons, we will refer to these regions as cold spots even though more recent observations [5, 6, 7] support their kinetic temperatures being the same as the rest of the polar cap. A general lack of correlation between cold spots and Mars Global Surveyor (MGS) Mars Orbiter Laser Altimeter (MOLA) measurements of clouds and Thermal Emission Spectrometer (TES) spectra suggest that most of the cold spots are surface regions of low emissivity. Occasionally, there are correlations to extremely dense polar night clouds and the "coldest" of the cold spots, suggesting a few of these cold spots may be "dry ice blizzards" in progress [6].

The MGS TES observations, combined with spectral modeling [5,7] using new CO₂ optical constants [8], illustrate that the "cold spots" are due to fine-grain CO₂, which cause a decrease in the 25 μm emissivity. Spectral models predict that fine-grain CO₂ (hereafter referred to as snow, regardless of the formation process) has high albedo and low emissivity in the 25-μm-transparency band. Coarse-grained CO₂ (hereafter referred to as ice) has low albedo (perhaps even transparent if the dust content is low) and near unit emissivity. Increasing the dust content in the CO₂ results in a large decrease in albedo, but only a slight increase in emissivity. TES observations have shown these effects [9] for the southern springtime season cap, suggesting that the bright outliers (e.g. the Mountains of Mitchel) are snow covered, while other areas (e.g. the cryptic region) are mainly composed of ice.

The purpose of this paper is to present results from the MGS TES continuing mission, showing the distribution of CO₂ snow and ice in space and time. The dense coverage of the Mars polar regions by MGS TES has provided the ability to monitor the seasonal variations of condensates. Because TES has three subsystems, we can monitor the distribution of solid CO₂ in two ways: (1) monitoring the spectral differentiation between snow and ice and (2) the estimation of local CO₂ mass accumulation.

The TES solar bolometer, combined with synthetically derived brightness temperatures, can differentiate between snow and ice [9]. The difference between the estimated surface kinetic temperature, T₁₈, and the brightness temperature in the CO₂ 25 μm transparency band, T₂₅, effectively measures the emissivity at 25 μm and is taken as an indicator of the grain size of CO₂ frost [5,6,9]. We will use the same convention as Titus et al. [6] where ice is defined as $\Delta T = T_{18} - T_{25} < 5$ K. This measure can be influenced by the presence of atmospheric dust, however that effect has not yet been quantified.

The TES directly measures the total reflected and emitted radiation, which in turn allow for the measurement of the geographic variation of the net radiation balance and, through integration of the inferred sublimation rates, the annual solid CO₂ budget. We use the sublimation budget instead of the condensation budget to minimize the impact of lateral transport of heat during the polar night [5, 10]

Data: The MGS spacecraft orbit has an inclination of 93°, ascending (going north) on the night-side and going south (descending) on the dayside with a 14-hour Mars local time (H) equator crossing. For simplicity, we will refer to TES observations acquired on the ascending leg as AM and those acquired on the descending leg as PM. In normal mapping nadir-oriented mode, TES sweeps a 9 km wide swath along the sub-spacecraft track, which is almost parallel to meridians except near the pole. In this observation mode, the times between repeat coverage is highly dependent on latitude, ranging from only a few hours along the "polar rings" at ± 87° latitude to several days at ± 60° latitude. This allows detailed analysis of spatial and temporal changes near the polar caps. However, at more equatorial latitudes seasonal analysis of specific locations is restricted due to the lengthy repeat time, approaching hundreds of days near the equator.

The TES data used were binned spatially into a polar stereographic projection with a mean resolution of 60 km per cell. Temporal binning was done on a base of 12 orbits (approx 23.55 hours). Missing data in the latitude/season cells were filled by linear interpolation in time.

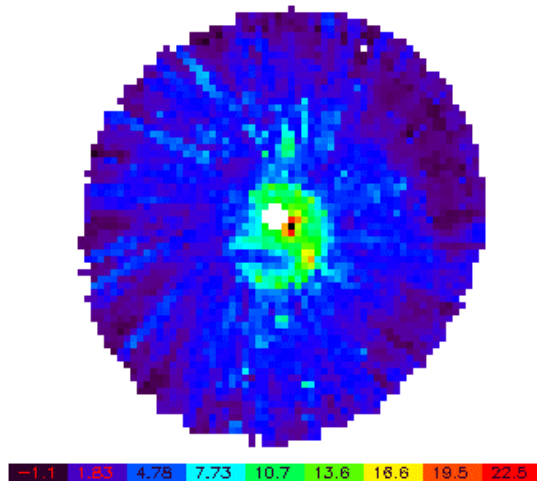


Figure 1: North polar grain-size index, ΔT , at $L_s = 342^\circ$. All polar figures have the same scale where the outer limits are at 45° latitude. The white plus in the center of the image is pole. Areas off the polar cap are white.

Snow and Ice Distribution:

North Polar Distribution. The winter (or condensation phase) cap is generally characterized by the observed $25 \mu\text{m}$ brightness temperatures (T_{25}) near the expected surface temperatures for solid CO_2 , suggesting that direct surface condensation as slab ice occurs. Kieffer and Titus [5] and Titus et al. [6] show that cold spot observations, strong indicators of snow, are restricted to the perennial cap and other localized topographical features, e.g. craters. We conducted a space-time analysis; our latest analysis is consistent with these prior results. The perennial cap has a high frequency of cold spot occurrence from approximately at $L_s = 200^\circ$ to approximately at $L_s = 350^\circ$.

The springtime (or sublimation phase) cap is generally characterized by low ΔT , suggesting slab ice. However, by $L_s = 45^\circ$ a bright ring has formed just inside the receding cap edge. [Fig. 2] This bright ring is not visible in the ΔT image, suggesting that the brightening is not due to CO_2 grain size effects. One plausible source of this bright receding ring is that water released from the season cap edge is redeposited as frost inside the cap [11].

During this same period of time, the perennial cap also appears bright without a corresponding increase in ΔT .

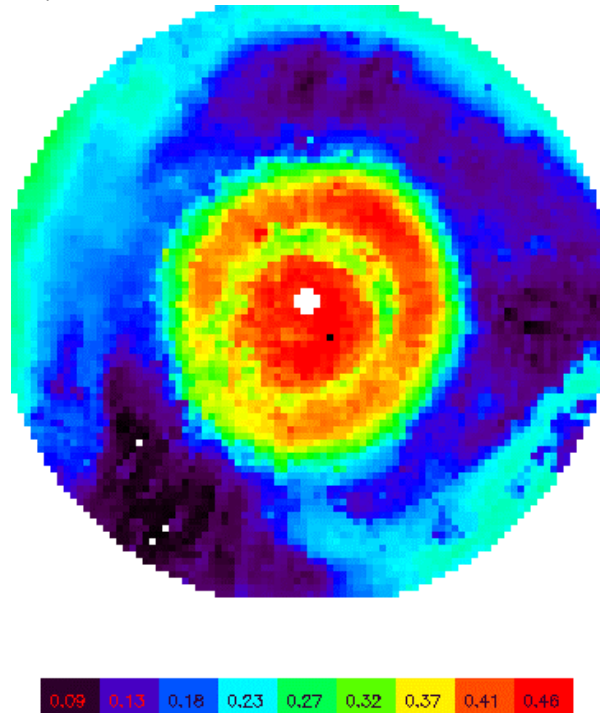


Figure 2: North polar cap albedo and grain-size index at $L_s=38^\circ$. There is a lack of correlation between these two parameters, suggesting that the brightening of the cap is due to water frost, not fracturing of CO_2 .

South Polar distribution: Cold spot activity in the southern winter starts approximately $L_s=16^\circ$. The Mountains of Mitchel is one of the most active regions. Cold spot activity continues until approximately $L_s=150^\circ$. After the sun has risen above the horizon, the cap begins to brighten, with the areas closest to the edge brightening first. A similar effect is

seen in ΔT , suggesting that the albedo brightening is due to an effective grain-size of the surface CO_2 grain-size. Paige [12] explained this phenomenon as the fracturing of the surface ice due to insolation. TES observations are consistent with this explanation.

In many cases, the brightest springtime regions were areas of greatest winter cold spot activity. Perhaps wintertime accumulation of snow increases the likelihood that fracturing occurs in the spring.

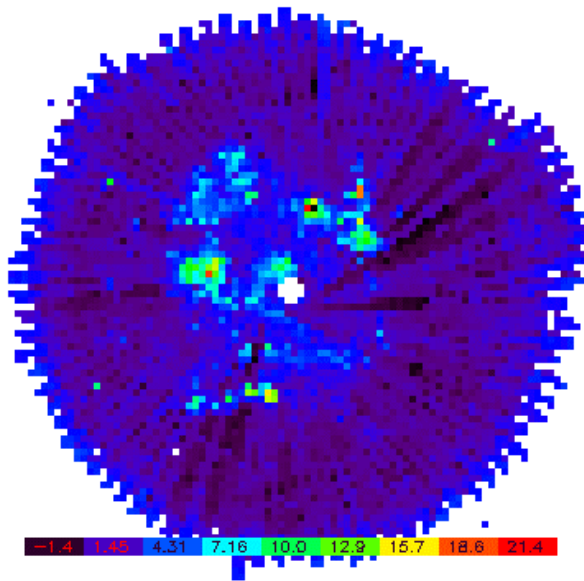


Figure 3: South polar cap grain-size index at $L_s=86^\circ$. The Mountains of Mitchel is one of the areas with high ΔT , suggesting the presence of snow.

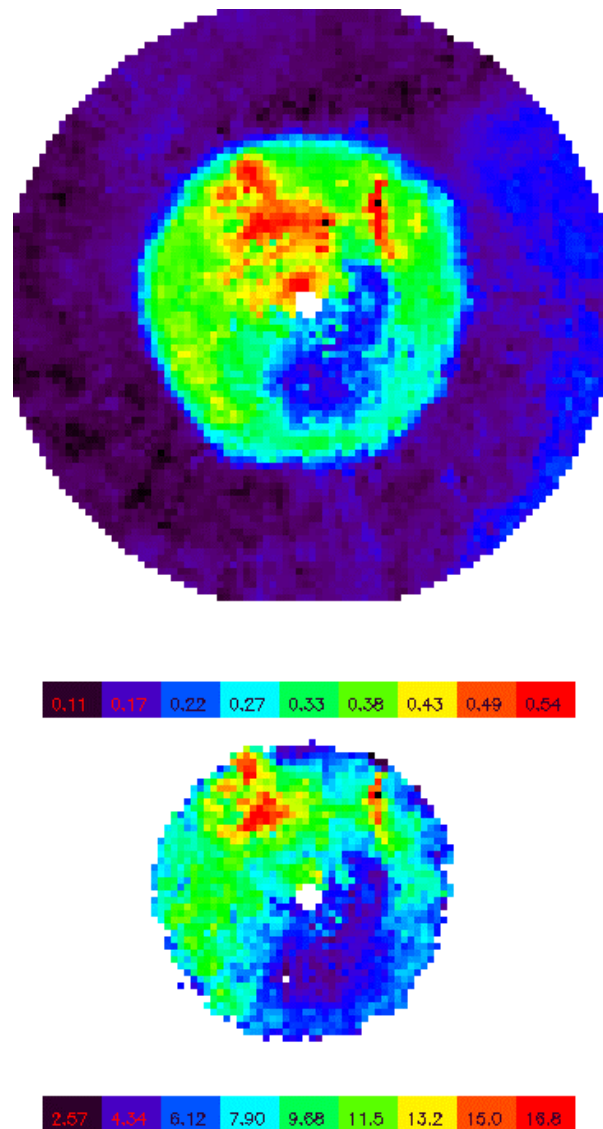


Figure 4: South polar albedo and grain-size index at $L_s=217^\circ$. Bright albedo areas generally have high ΔT , while areas with low albedo tend to have low ΔT .

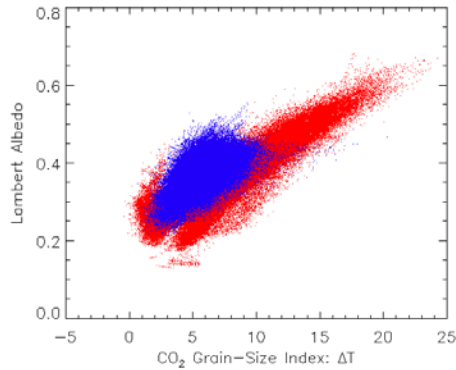


Figure 5: Albedo vs. CO₂ grain-size index. The data were restricted to springtime data with surface temperature less than 160 K. The red dots are for the south polar cap and the blue dots are for the northern polar cap.

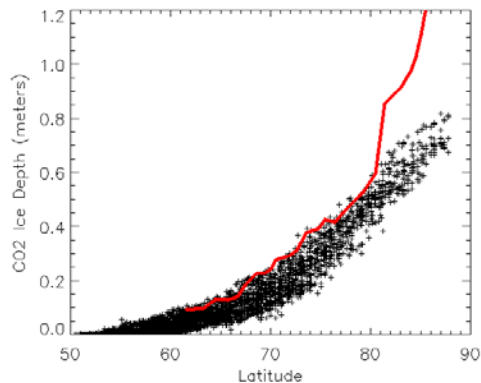


Figure 6: North polar seasonal cap depth estimates. The black pluses are seasonal cap depths estimated from TES mass-balance calculations, assuming a CO₂ density of 1606 kg/m³. The red line is an estimate from MOLA.

CO₂ Mass Budget: The underlying assumptions in the TES mass balance calculations are that the total energy input into Mars is characterized by the solar bolometer and that the total energy out of the Mars system is characterized by the thermal bolometer. The energy difference between the input and output is assumed to be due to the sublimation or condensation of CO₂. This implies that there is no geothermal heating or lateral transport of heat through the atmosphere. While initial estimates suggest that geothermal heating is negligible, a comparison of condensation and sublimation mass budgets suggest that a large amount of heat transport does occur during the polar night [5,10]. However, comparisons of the sublimation budget to other observations [13] suggest that this technique is a

good estimate of actual amount of CO₂ in the springtime seasonal caps. For a detailed description of how the mass balance calculation is done, see Kieffer et al. [5] Figure 6 shows the estimated depth of seasonal CO₂ if one assumes a pure substance ($\rho = 1606 \text{ kg/m}^3$) compared to the seasonal depth estimated by MOLA [13]. If one assumes that the MOLA estimates are correct, we estimate the density of ice (latitudes south of 80°N) as $1107 \pm 150 \text{ kg/m}^3$ and the density of snow/ice mixture (latitudes north of 80°N) as $979 \pm 133 \text{ kg/m}^3$. The south polar MOLA depth estimates are not presented here because of possible systematic errors in their depth estimates. When comparing MOLA and TES estimates, this offset must be $\sim 20 \text{ cm}$ to bring southern density estimates into agreement with the density for northern ice. A 20 cm offset is consistent with possible systematic errors for the southern data [14]. While these density estimates are preliminary, they are consistent with TES spectral observations of snow and ice distributions.

Conclusions:

- The predominate form of CO₂ condensation is direct surface condensation as slab ice.
- Regions with a high frequency of snow deposition during the winter generally have brighter than average albedo in the spring, e.g. the Mountains of Mitchel.
- Springtime brightening of the south polar cap is predominately a change in grain size of the CO₂. This is not the case for receding northern cap. Albedo variations are most likely dominated by the presence of water frost.
- An estimate of martian northern CO₂ ice and snow/ice mixture densities based on combining TES mass balance calculations and MOLA seasonal elevation changes are $1107 \pm 150 \text{ kg/m}^3$ and $979 \pm 133 \text{ kg/m}^3$, respectively.

References:

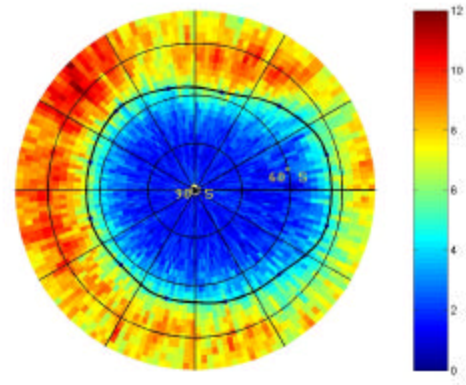
- [1] Leighton R. and Murry B. (1966) *Sci.*, 153, 136-144. [2] Forget F. and Pollack J. (1996) *JGR*, 101, 16865-16879. [3] Tillman J. et al. (1993) *JGR*, 98, 10963-10971. [4] Kieffer H. et al. (1976) *Sci.*, 193, 780-786. [5] Kieffer H. and Titus T. (2001) *Icarus*, 154, 162-180. [6] Titus T. et al. (2001) *JGR*, 106, 23181-23196. [7] Hansen G. (1999) *JGR*, 104, 16471-16486. [8] Hansen G. (1997), *JGR*, 102, 21569. [9] Kieffer H. et al. (2000) *JGR*, 105, 9653-9699. [10] Titus T. (2003) *Mars Atm. Workshop*, Granada, Spain. [11] Kieffer H. (2002) *AGU Fall Mtg.*, Abstract P72C-02. [12] Paige D. (1985), *PhD Thesis*. [13] Smith D. et al. (2001) *Sci.*, 294, 2141-2146. [14] Smith D. *Personal communication*.

Correlation of Neutron-Sensed Water Ice Margins with Topography Statistics. R.L.Tokar¹, M.A. Kreslavsky^{2,3}, J.W.Head, III³, W.C. Feldman¹, K.R. Moore¹ and T.H. Prettyman¹, ¹Space and Atmospheric Sciences, MS D466, Los Alamos National Laboratory, Los Alamos, NM, 87545, rlt@lanl.gov, ²Kharkov Astronomical Observatory, Kharkov, Ukraine, ³Department of Geological Sciences, Brown University, Box 1846, Providence, RI, 02912.

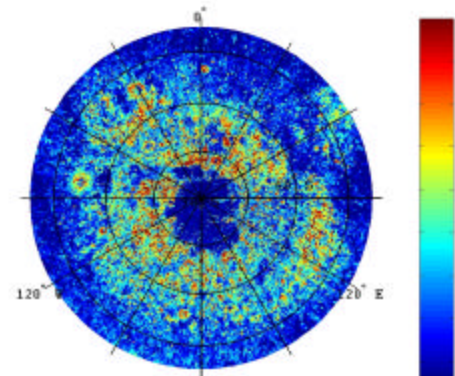
Introduction: In [1], surface roughness and curvature obtained from high resolution MOLA data are used to characterize a sedimentary mantle at high Martian latitudes, (poleward of $\sim 40^\circ$ - 60°). The equatorward boundary of the mantle correlates with the locations of dissected terrain identified in MOC images [2]. The dissected terrain in [2] is thought to be degraded water cemented soil, and the mantle discussed in [1] is inferred to be water ice rich. This conclusion is given further support in [3], where a positive correlation of the results in [1] and [2] is made with Odyssey neutron sensing of high hydrogen content in the near surface soil at high southern latitudes. The Odyssey data are measured by the neutron spectrometer (NS) component of the gamma ray spectrometer (GRS).

In this study, the margins between the water ice rich mantle and the relatively dry equatorial region are studied for the northern and southern hemispheres using the Odyssey NS data and the MOLA roughness/curvature data. The position and extent in latitude of the margin is estimated via simulations of the NS data and the results are compared with average MOLA topography statistics. Preliminary results for two bands of longitude (120° - 150° W and E) in the southern hemisphere are reported here.

Results: The following figure shows a map of the epithermal ($0.4 \text{ eV} < E < 700 \text{ keV}$) NS counting rate measured over the south circumpolar region during southern summer, as in [3]. Recall that low epithermal neutron count rate (blue region) corresponds to high hydrogen content of the near surface soil. See [4] for a complete overview of NS hydrogen estimates both at the poles and in the equatorial region. The black curve is the nadir position of Odyssey when the epithermal counting rate falls to $\frac{1}{2}$ the maximum measured before encountering the water ice rich region. The margin region studied here is the transition region near the black curve that delineates the water rich circumpolar mantle from the relatively dry equatorial region.

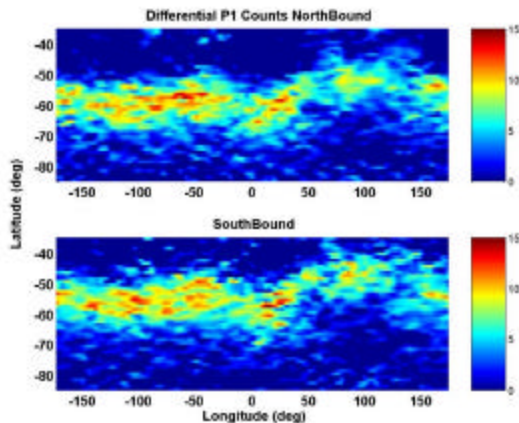


The following figure is a map of MOLA -derived 0.6 km curvature, calculated as in [1]. Mapped is the ratio of the median curvature to the interquartile width of the curvature-frequency distribution. The water ice rich mantle exhibits a prevalence of concave (> 128) as opposed to convex (< 128) curvature. As established in [3], the equatorward boundary of the ice mantle is in qualitative agreement with the NS boundary shown above, although the boundary obtained from the curvature often lay equatorward of the NS boundary.

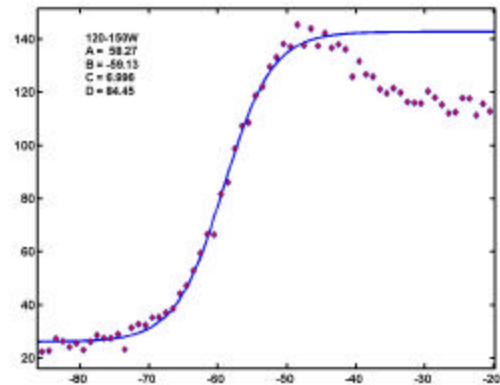
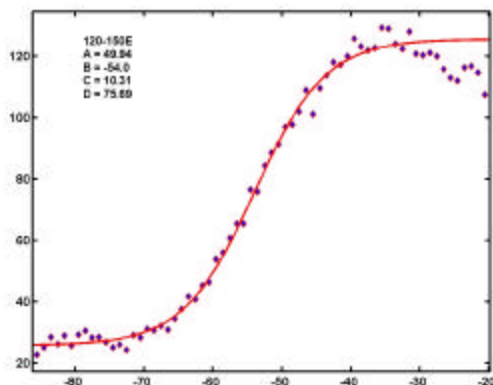


The figure below illustrates the gradient in epithermal neutron counting rate with latitude (counts/s/deg). Where the gradient is large and localized in latitude the margin is sharp whereas an extended margin has a relatively smaller gradient distributed over an extended range of latitude. The top frame corresponds to northbound Odyssey orbit segments, the bottom southbound, although this distinction will not be used in our preliminary analysis. Here we concentrate on the two longitudinal segments, -120° to -150°

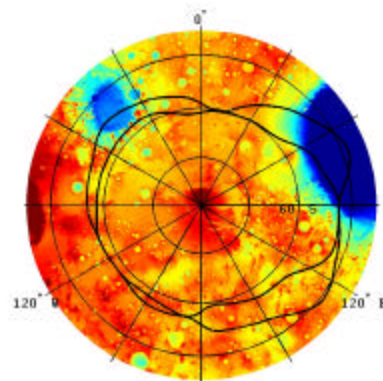
(west) and 120° to 150° (east). These regions have relatively small altitude variations, thereby simplifying the analysis of the NS data, as opposed to regions near the Hellas or Argyre basins. For both orbit directions, the gradient illustrates that for the west slice the margin between the water ice and dry soil is relatively sharp, while that in the east extends over a larger range in latitude.



This point is illustrated further in the following two figures. Shown are averages of the NS count data over 30 degree longitude bins. The first is for the segment 120° - 150° E, the second 120° -150° W. The average NS epithermal counts in 19.6s are shown (data points), as are fits to the data (solid curves). The data is fit to the equation $A * \tanh((\text{latitude}-B)/C) + D$, with B a measure of the center of the margin and $2 * C$ the characteristic width of the margin. For the east slice, $B = 54^\circ\text{S}$ and $C = 10.31^\circ$. For the west $B = 59.13^\circ\text{S}$ and $C = 7.0^\circ$, supporting the conclusion that the margin for the east slice is extended and the west slice sharp.



This observation is quantified by simulating the NS data for various models of the margin, using the simulation model described elsewhere [3], [5]. The simplest model assumes that the margin region is a uniform mix of the circumpolar water ice and dry equatorial soil. This yields the results shown in the following figure, where the estimated margin position is overlaid on MOLA topography. We perform this analysis at all longitudes, neglecting corrections to the NS counting data due to topography within the basins. The ice/dry margin region is between the black curves, and at latitudes where the curves coincide the NS data is consistent with a step discontinuity from water ice to dry soil. Due to the extent of the detector footprint (~ 10 deg FWHM) about the Odyssey nadir, the simulation model suggests that the detector can not distinguish between margins $< \sim 7^\circ$ in latitude. Note in this figure that the conclusions obtained from the gradient in NS counts and the fits to the counts with latitude are substantiated, namely that the margin is extended over the 120°-150° E slice and sharp over the 120°-150° W slice.

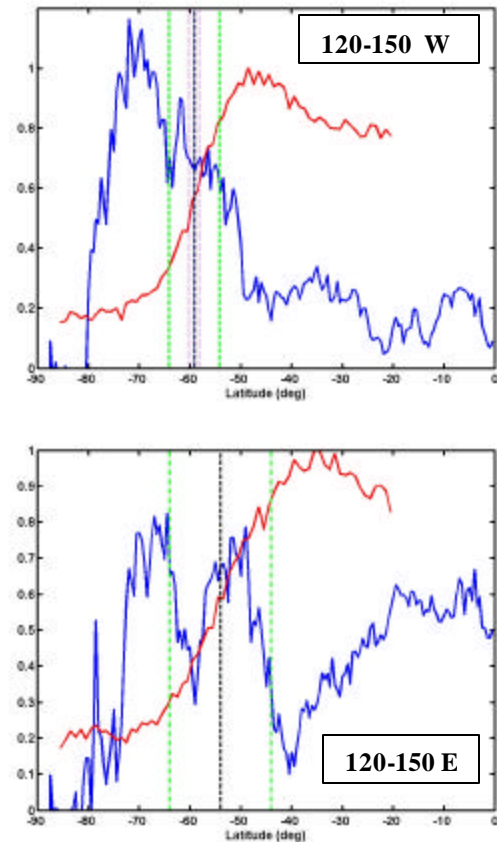


A more accurate model for the water ice margin than the 50/50 mixture of water ice and dry soil is one

where the depth of the water ice below the surface decreases within the margin with decreasing distance from the pole. This is motivated by simulations yielding the depth to ice stability, e.g. [6]. We have performed a series of NS system simulations for margins with variable width in latitude; the source model in the simulation has three surface components, the water ice rich circumpolar mantle under a thin layer of dry dust, the margin with linearly varying ice depth that decreases in the poleward direction, and the dry soil equatorial region. The simulation results for the NS counting rate variation with latitude are fit to tanh functions, as above.

The following two figures illustrate the comparison of the NS data, the MOLA 0.6 km baseline curvature data, and the NS simulation results for both the 120° - 150° W (top) and E (bottom) slices. The red curve is the normalized NS epithermal neutron counting rate and the blue curve is the bin-averaged and normalized MOLA 0.6 km curvature. The vertical dashed lines are results of the simulations, with the black dashed line the center of the margin ("B") and the green dashed lines at $B \pm C$ degrees.

First note that, especially in the case of the sharp 120°-150° W slice at the top, the MOLA -derived curvature data shows the transition to the concave mantled topography almost exactly where the NS epithermal counts begin a sharp decrease. Although the details will be strengthened by further study for all longitudes and for the northern hemisphere margin, it appears that the MOLA curvature shows the concave ice mantle signature well into the NS sensed margin. Note that the margin center from the NS data is at $\sim 59^\circ$ S for the west slice and further that the uncertainty in this location is at most 1 or 2 degrees. Note that in the case of the west slice the NS can not distinguish between a step discontinuity and the extended margin between the green dashed lines. In the case of the east slice, again the NS counts begin to decrease almost exactly where the concave topography becomes more prevalent. However, the situation is more complicated both within and equatorward of the margin. Inspection of the margin suggests that the signature of concave/convex curvature may be quantitatively related to the mixture of ice and dry soil regions within the NS footprint. However, both the mantling process and the underlying geology influence the curvature.



References:

- [1] Kreslavsky, M.H. and J.W. Head (2002) *GRL*, 29, 10.1029/2002GL015392.
- [2] Mustard J.F. et al. (2001) *Nature*, 412, 411-414.
- [3] Tokar R.L. et al. (2002) *GRL*, 29, 10.1029/2002GL015691.
- [4] Feldman, W.C. et al., 2003, this meeting.
- [5] Tokar R.L. et al., *GRL*, submitted March, 2003.
- [6] Mellon, M.T. and B.M. Jakosky, (1993) *JGR*, 98, 3345-3364.

LOW-TEMPERATURE AQUEOUS ALTERATION ON MARS: INSIGHTS FROM THE LABORATORY.

N. J. Tosca, S. M. McLennan, D. H. Lindsley and M. A. A. Schoonen, Department of Geosciences, State University of New York at Stony Brook, Stony Brook, NY 11794-2100 (Nick@pbisotopes.ess.sunysb.edu)

Introduction: The soil-like material mantling the Martian surface is geologically and chemically complex and holds information of past and present climatic conditions on Mars. Present knowledge of this surface material suggests that low-temperature, aqueous alteration may have been a major factor in forming the material that has been sampled thus far by the Viking and Pathfinder landers. The term aqueous alteration used here, encompasses a wide range of processes and includes both dynamic and stagnant water-rock and gas-rock alteration mechanisms. Much effort has gone into characterizing this material, and several models, based on a wide range of evidence, have given rise to many processes and resultant mineral/mineraloid phases that may be (or have been) of importance on the surface of Mars.

In terms of low-temperature aqueous alteration, the primary material being altered, that of the Martian basaltic crust, is somewhat constrained but the aqueous processes are not. The secondary alteration phases resulting from such processes have most likely been subject to sedimentary and physical mixing processes and as a consequence are well homogenized, somewhat obscuring their chemical signatures. Therefore, it is indeed a complicated and difficult problem to address the role that low-temperature aqueous alteration may have played in the formation of the Martian soil.

One way to approach such a problem is to do so experimentally. Experimental results from aqueous alteration experiments can highlight the most important chemical processes in a given system and the relevance of the laboratory system to a potential model can be assessed. Some workers have taken advantage of terrestrial systems, which have been used as templates for alteration on Mars. However, new constraints on Martian surficial processes can be made by testing these models experimentally by taking advantage of the present knowledge of the primary Martian basaltic crust.

A major conclusion of this work is how, among several other factors, aqueous alteration is highly dependent on primary starting material. In this paper, recent results of alteration experiments with synthetic basaltic material will be evaluated and their relevance to the Martian surface will be discussed.

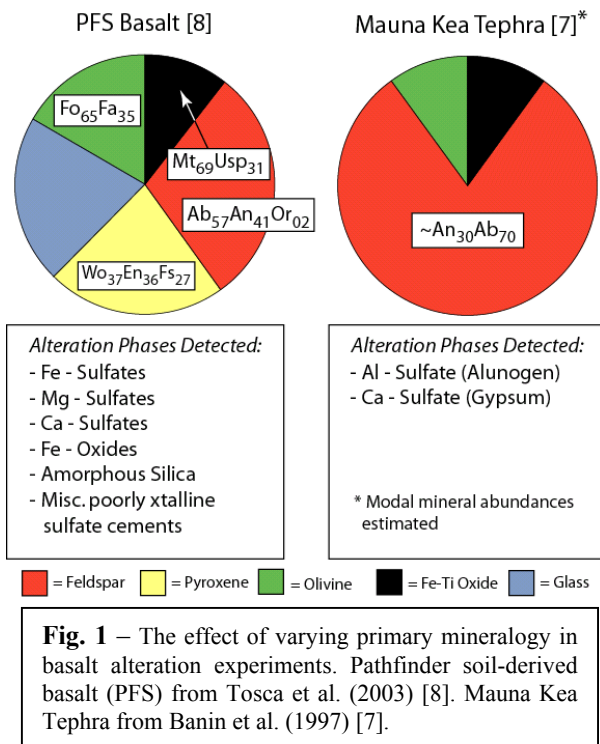
Low Temperature Aqueous Alteration on Mars: Several approaches to low temperature aqueous alteration on Mars have been taken to understand the origin

of the surface material as well as past climatic conditions on that planet.

The first of the major models for low temperature aqueous alteration on Mars includes palagonitization, which was first suggested by Gooding and Keil in 1978 [1]. The term palagonitization generally refers to the formation of palagonite, a hydrated, amorphous and isotropic alteration product of mafic glass [2]. The exact nature of palagonite, both chemically and mineralogically, is poorly defined and can contain a wide range of secondary, poorly crystalline minerals, most of which are combinations of smectites [2]. The initial gel-like palagonite is metastable, and over time may evolve into crystalline products such as clays, zeolites, oxides and carbonates [2]. The precipitation of palagonite and its associated poorly crystalline phases is dependent on many factors, which are important for other mechanisms of low temperature aqueous alteration as well and are discussed below. Palagonitization has been suggested to be important on Mars due to both the spectral similarities of palagonite material to the bright regions of Martian soils and the possibility that basaltic glass is somewhat abundant on the surface of Mars. In light of these observations, numerous studies have characterized terrestrial palagonites as analogs to Martian soil [e.g., 3-5].

Another major model for low temperature aqueous alteration on Mars is the acid fog model. This model involves the interaction of volcanically derived acidic volatiles with the Martian basaltic crust [6]. These volatiles may interact with primary rock in low fluid-rock ratios, causing mineral/glass dissolution. Subsequent evaporation of the fluid at a far-from-equilibrium state results in poorly crystalline alteration products which are composed mainly of sulfate and chloride salts. This model is proposed to have taken place in relatively recent Martian geological time (up to 1Ga) and its purpose is to explain the nature of the uppermost layer of surface material on Mars. This model was first experimentally tested in the laboratory by Banin et al. [7], who reacted Mauna Kea tephra with various acid mixtures and reported the precipitation of Ca and Al salts detectable by XRD. Tosca et al. [8] have further tested this model using synthesized basalt and glass with Pathfinder-derived bulk compositions and found that varying the starting material and aqueous conditions used in these experiments, significantly varies the secondary alteration minerals formed in this process. Figure 1 provides an example of the different alteration minerals Tosca et al. formed by

varying the primary mineralogy of the basalt. This approach and the putative alteration phases formed as a result, illustrates the importance of several different factors in low temperature aqueous alteration studies applied to Mars and will be discussed below in greater depth.



Brine interactions with the surface of Mars and their potential to form evaporites has been another suggested mechanism of alteration [9]. For example, the soluble salts found in nakhlites have been interpreted to result from evaporitic conditions on Mars [10]. One experimental study aimed at brine interaction on Mars was conducted by Moore and Bullock [11], where CO₂ charged water was interacted with SNC mineral mixtures for a period of one year. Modeling evaporation of the resulting fluid predicted Ca-sulfates, Al-hydroxide and carbonates.

Studies involving the importance of weathering on the surface of Mars also include a study by McSween and Keil [12], who evaluated chemical systematics of the Pathfinder and Viking soil data. The chemical trends produced by both palagonitization and the acid fog experiments performed by Banin et al. [7] were evaluated and it was determined that the chemical trend resulting from palagonitization may provide a suitable analogy to the Martian soils. However, McSween and Keil suggest that these changes are limited and that the soils contain components of different lithologies. Also, it has been suggested in this study and in others [e.g., 13] that complex sedimentary proc-

esses most likely have changed the compositions of the soils and that the homogeneous dust present on Mars may reflect the most abundant lithologies on the surface.

Other specific processes or secondary alteration phases, which may be important during low temperature alteration, have been suggested. For example, carbonate formation has been suggested to be important on Mars, despite little evidence for carbonates at the surface. The postulation of high partial pressures of atmospheric CO₂ at one time in the past have led to the suggestion of carbonate reservoirs acting as a sink for CO₂ [e.g., 14].

Sedimentary silica is another example of potentially important secondary alteration phases and has been suggested by McLennan [15], who notes that silica is highly mobile during basalt alteration and that secondary silica phases may have been formed and subsequently distributed in sediments. In light of this observation, McLennan suggests that this may explain some of the high silica features observed on Mars.

The origin of pre-terrestrial secondary alteration materials present in SNC meteorites has been studied experimentally by Baker et al. [16] and provides an example of basalt alteration in experimental settings. In this study, CO₂, S and Cl rich waters were passed over crushed Columbia River basalt at two different temperatures, 23 and 75°C. The low temperature experiments formed calcite, magnesite and opal-CT. Resulting fluid compositions were also modeled for equilibrium evaporite assemblages.

Laboratory Systems – Insights from Synthetic Basalt Alteration: The models discussed have several aqueous geochemical processes in common and it is important to determine what these processes are as well as the factors that govern them. Using synthetic basalts and basaltic glass of Martian composition as a starting point for aqueous alteration has begun to provide important information about fundamental aqueous processes involved with basalt alteration of such a chemically unique host rock. These processes and supporting observations from the laboratory are discussed in this section.

Similar to how a rock is defined as an aggregate of minerals, aqueous basalt alteration can be defined as an aggregate of mineral alteration processes. The contributions to an aqueous system from the alteration of individual mineral/glass phases can vary significantly. Therefore, the fluid chemistry and resultant secondary minerals formed will be a direct result of the primary phases being altered. Although there are countless factors involved in aqueous environments, the discussion here is limited to those that are common among the major models proposed for the Martian surface. These include dissolution and its effect on fluid chem-

istry, and precipitation processes forming secondary alteration phases.

Dissolution: Interaction of basalt with fluids in most systems results first in dissolution. Dissolution is a major process in low temperature alteration, because dissolution rates and mechanisms largely determine fluid chemistry. The dissolution rates and mechanisms of mafic minerals and glasses differ significantly from each other and are dependent on several processes, including temperature, fluid composition, fluid dynamics and the structure of the material being dissolved. Variation of these factors has the potential to change dissolution rates by orders of magnitude. Laboratory investigations using synthetic basalt have shown that in low temperature static-fluid systems, the stoichiometry of dissolution is mainly dependent on acid concentration [8]. In systems with low pH values, dissolution proceeds stoichiometrically, releasing the components of the mineral/glass in to solution in the same proportions as the solid. As pH rises and becomes less aggressive but still acidic, dissolution proceeds non-stoichiometrically, where some components are released preferentially to others. This is the case in most natural waters on Earth and as a consequence, is a key factor in determining fluid composition.

Non-stoichiometric dissolution is controlled significantly by the crystal chemistry of the phase being dissolved. Silicate minerals dissolving non-stoichiometrically readily release ionically bonded non-structural constituents. Dissolution of orthosilicates such as olivine liberates Fe^{2+} , Mg^{2+} and H_4SiO_4^0 rapidly, due to the breaking of either Mg-O bonds or Fe-O bonds, which can destroy the entire structure of the mineral [17]. Under oxic conditions where Fe^{2+} may be oxidized to Fe^{3+} , which is insoluble, dissolution may proceed non-stoichiometrically. In framework silicates such as feldspars, the K^+ , Na^+ and Ca^{2+} ions are released initially, while the aluminosilicate framework is hydrolyzed and destroyed at a much slower rate. The destruction of the residual framework is also dependent on the amount of Al present, as Al-O bonds are broken more easily than Si-O bonds [17]. In pyroxenes, cations occupying the M2 sites are preferentially released during this process. This can include Ca^{2+} , Fe^{2+} and Mg^{2+} , depending on the chemistry of the pyroxene. The residual structure of the pyroxene is then composed of M1 cations cross-linking chains of silicate tetrahedra. Destruction of the residual layer then proceeds by the breaking of M1-O bonds and Si-O bonds.

In basaltic glass, network-modifying cations such as K^+ , Na^+ , Ca^{2+} , Mg^{2+} , Mn^{2+} and Fe^{2+} are released preferentially to network-forming cations such as Si^{4+} , Al^{3+} , Ti^{4+} and Fe^{3+} . Basaltic glass dissolution is dependent on the Si content present in the glass. Higher

Si content causes a higher degree of polymerization and therefore, decreases the rate of dissolution substantially of both network-forming and modifying cations. This observation is important in that if the Type 2 terrain on Mars contains a primary high-silica glass component [18], element mobility and susceptibility of that primary material to chemical weathering would be significantly less. Laboratory observations have shown a decrease by a factor of 2000 in basaltic glass dissolution rate by increasing SiO_2 content in the glass from 48.8 wt. % to 57.8 wt. % [19]. The non-stoichiometric release of network modifying elements forms a residual leached layer, rich in structural silica and aluminum, which is destroyed at a much slower rate.

Feldspars, pyroxenes and basaltic glass have significantly different rates of dissolution and if this dissolution is non-stoichiometric, often form leached layers at the surface, rich in residual structural silica and aluminum, which are both relatively insoluble in acidic fluids. The presence of this leached layer is therefore common with basalt alteration and may also be a common process on Mars. Upon fluid evaporation, a process common among most models of soil formation on Mars, the thickest leached layers formed in our experiments craze and spallate. This may be important in that the leached layers may be released in to the Martian sediment and be redistributed as essentially amorphous silica, exposing fresh mineral and glass surfaces to alter. The reactivity of such a leached layer has been documented in that the pH of pore waters in this layer have a substantially higher pH than the bulk solution, which is conducive to precipitation of secondary phases inside the depleted layer [20]. Also, it may easily acquire negative surface charge and cause adsorption of aqueous constituents on to this layer [20]. Finally, the leached layer may also recombine and polymerize to form small amounts of phases such as clays, if enough aqueous constituents are available in the fluid [20].

Controls on fluid chemistry: Using basaltic compositions relevant to Mars, we observe that primary mineral phases each control different aspects of fluid chemistry. For example, Na^+ , K^+ and Ca^{2+} are ubiquitous in initial fluid compositions, due to their soluble nature and their weaker bonding in feldspars, pyroxenes and basaltic glass. The chemistry of Mg in these fluids is more complex. For example, forsteritic olivine is observed to dissolve the quickest in synthetic basalt alteration experiments, releasing large amounts Mg^{2+} and H_4SiO_4^0 into solution. This in turn raises the state of saturation with respect to amorphous silica as well as Mg- SO_4 phases, if fluids are rich in SO_4^{2-} . Magnesium from pyroxenes, however, may be released but kinetically inhibited, due to its preferential

M1 site occupancy and stronger bonding characteristics. Magnesium rich pyroxenes, such as enstatite, may be able to release significant amounts of Mg from the M2 site. This release is most likely limited to the first stages of alteration, in that a silica-rich depleted layer may soon form to retard dissolution. Therefore, in kinetically restricted models of alteration, olivine may be controlling the Mg^{2+} in the fluid as opposed to pyroxenes. Ferrous iron may also behave in this way, but results from synthetic basalt alteration experiments show that Fe^{2+} release from pyroxenes is much more significant than Mg^{2+} release in initial stages of alteration. With large amounts of Fe^{2+} being released into solution from pyroxenes and olivine, the fate of Fe^{2+} in solution remains uncertain because Fe^{2+} oxidation mechanisms are unconstrained. There are several pathways by which Fe^{2+} could be oxidized and in our synthetic alteration experiments exposed to the Earth's atmosphere, oxygen is the most important oxidant, producing secondary ferric phases as grains and coatings. More studies remain to be done to determine potential oxidants of Fe^{2+} on the Martian surface. Solid state iron oxidation of ferrous silicates and oxides [21] remains another possible mechanism for production of secondary ferric phases on Mars, but has been largely unexplored in this context.

Precipitation: The precipitation of minerals from various fluids depends on several factors. Among the most important factors observed in our experiments are the saturation state of the alteration mineral and the structure of both the precipitating mineral as well as the substrate on which it precipitates. Several experiments performed with synthetic basalt have shown large amounts of poorly crystalline alteration minerals precipitating on the surfaces of minerals and glasses. The initial phases are metastable or amorphous phases, which most likely have a higher rate of nucleation than subsequent stable phases, due to their wide-spread occurrence and poor crystallinity [22]. This process is referred to as Ostwald ripening and models such as palagonitization are dependent on such a process [2]. For example, the initial alteration phases precipitated during the formation of palagonite will most likely be metastable with respect to common alteration materials such as smectites observed in more advanced aging of palagonite.

Conclusions: Models for formation of the Martian soil share common fundamental aqueous processes, which are dependent on several factors prevailing on the surface. It is important to understand what these processes are and how they may be important during low temperature aqueous alteration. Several of these alteration processes begin with dissolution of primary mineral phases and are dependent on the chemistry of

the minerals themselves. Therefore, when testing models of low temperature aqueous alteration on Mars, relevant starting material is one of the most important factors. A wide variety of robust, analytical resources are also needed to characterize the chemical processes operating in laboratory systems, because microscopic observations in many cases, have global implications.

The discussion presented here is the result of the first stage of a large-scale approach to understanding the surficial processes on Mars experimentally. Many questions have been raised in light of recent observations and therefore, much work is needed to place further constraints on the origin of the Martian soil. More models for soil formation will be tested using even more starting materials, aqueous environments and experimental and analytical methods. The capability of synthesizing compositionally accurate starting material as well as adjusting experimental and analytical methods accordingly will result in observations aimed at a wide variety of microscale and macroscale processes that may be of importance for the surface of Mars. New constraints from future missions of Martian exploration will be used in our approach in further refining our understanding of the Martian surface material.

References: [1] Gooding, J.L. and Keil, K. (1978) *Geophys. Res. Lett.*, 5, 727-730. [2] Stroncik, N.A. and Schmincke, H.-U. (2002) *Int. J. Earth Sci.*, 91, 680-697. [3] Morris, R.V. et al. (2000) *J. Geophys. Res.*, 105, 1,757-1,817. [4] Morris, R.V. et al., (2003) *LPS XXXIV*, Abstract #1874. [5] Bell, J.F. et al. (1993) *J. Geophys. Res.*, 98, 3,373-3,385. [6] Banin, A. (1996) *Adv. Space Res.*, 18, 233-240. [7] Banin, A. et al. (1997) *J. Geophys. Res.*, 102, 13,341-13,356. [8] Tosca, N.J. et al. (2003) *LPS XXXIV*, Abstract #1325. [9] Bridges, J.C. and Catling, D.C. (2001) *Space Sci. Rev.*, 96, 365-392. [10] Bridges, J.C. and Grady, M.M. (1999) *Met. Planet. Sci.*, 34, 407-415. [11] Moore, J.M. and Bullock, M.A. (1999) *J. Geophys. Res.*, 104, 21,925-21,934. [12] McSween, H.Y. Jr. and Keil, K. (2000) *Geochim. Cosmochim. Acta*, 64, 2155-2166. [13] McLennan, S.M. (2000) *Geophys. Res. Lett.*, 27, 1,335-1,338. [14] Morse, J.W. and Marion, G.M. (1999) *Am. J. Sci.*, 299, 738-761. [15] McLennan, S.M. (2003) *Geology*, 31, 315-318. [16] Baker, L.L. et al. (2000) *Met. Planet. Sci.*, 35, 31-38. [17] Oelkers, E.H. (2001) *Geochim. Cosmochim. Acta*, 65, 3,703-3,719. [18] Bandfield, J.L. et al. (2000) *Science*, 287, 1,626-1,630. [19] Tosca, unpublished data. [20] Casey, W.H. and Bunker, B. (1990) *Rev. Mineral. Geochem.*, 23, 397-426. [21] White, A.F. (1990) *Rev. Mineral. Geochem.*, 23, 467-509. [22] Stumm, W. and Morgan, J.J. (1996) *Aquatic Chemistry*, Wiley, 1,022 p.

THE BEAGLE 2 ENVIRONMENTAL SENSORS: INTENDED MEASUREMENTS AND SCIENTIFIC GOALS. M. C. Towner¹, T. J. Ringrose¹, M. R. Patel¹, D. Pullan², M. R. Sims², S. Haapanala³, A.-M. Harri³, J. Polkko³, C. F. Wilson³, J. C. Zarnecki¹, ¹ PSSRI, Open University, Walton Hall, Milton Keynes, UK, m.c.towner@open.ac.uk, ² Space Research Centre, Dept of Physics and Astronomy, University of Leicester, University Road, Leicester, UK, ³ Finnish Meteorological Institute, Geophysical Research Division, P.O. BOX 503, FIN-00101 Helsinki, Finland, ⁴ Atmospheric, Oceanic and Planetary Physics, Clarendon Laboratory, University of Oxford, Parks Road, Oxford, U.K.

Summary: Beagle 2 is a 30kg lander for Mars, optimized for exobiology, launching in June 2003 as part of the European Space Agency (ESA) Mars Express mission[1]. The expected lifetime on the surface is 180 sols, with a landing site in Isidis Planitia[2]. One of the instruments on board is a suite of sensors for monitoring the local environment, and hence helping to determine if life could, or still can, exist there. The suite consists seven sensor subsystems weighing 153 grams, and due to the tight constraints of the Beagle 2 lander, primarily of simple analogue sensors, distributed over the lander. The suite has 2 major themes:

A meteorological package will record wind speed and direction, atmospheric pressure and temperature at a variety of heights, and look for particle saltation.

A life environment subsystem will measure the local radiation environment, the surface UV flux, and attempt to verify the presence of oxidants such as hydrogen peroxide, (without identifying the particular species present). Additional sensors will record the upper atmosphere density profile (determined by the acceleration encountered during probe entry and descent).

Introduction: Measurements of the local environmental conditions on Mars are a valuable tool as part of a lander's repertoire - both as independent measurements in their own right (for example meteorology), or providing context information which adds to the value of data from specific instruments (for example local temperature). The Beagle 2 lander, part of the Mars Express mission to Mars includes an array of sensors, designated the Environmental Sensors Suite (ESS), designed to monitor various local conditions. The sensors are designed to answer specific science goals, as well as providing support for the other on-board instruments.

Instrument description: The ESA Mars Express mission is due for launch in late May or early June 2003, arriving at Mars on 26th December 2003, initially braking into an elliptical orbit, 250km by 11,580km [1]. If all goes well, it will be at Mars at the same time as the ISAS spacecraft Nozomi and the NASA Mars Exploration Rovers, Mars Odyssey (and possibly Mars Global Surveyor if still active). The Mars Express scientific payload is described by Schmidt *et al.* [1]. The

Beagle 2 lander is due to land in the Isidis Basin, at 270°W and 10.5°N [2]. It has a landed mass of 30kg, and uses an airbag and parachute system for descent, with an intended primary mission lifetime of 180 sols on the surface.

Onboard Beagle 2, ESS will operate throughout the mission lifetime and is intended to study both short (seconds, minutes, days) and long term (seasonal) timescale variations in the local environment. It has 2 major themes:

1) Landing site meteorology, A major science goal of the meteorology program is to improve our understanding of the Martian dust cycle. High-frequency measurements will be used to characterize near-surface turbulence, and to make quantitative measurements of dust devils (convective vortices). These high-frequency measurements of potentially dust-raising winds are supplemented with a sensor which will estimate the momentum of saltated particles. Low-frequency meteorological measurements will provide a long-term meteorological record, enabling study of day-to-day and seasonal variation in weather patterns.

2) The astrobiological implications of the local radiation and oxidative environment. Since the major Beagle 2 payload instrument, GAP provides a comprehensive analysis of the chemical locale, it was decided to concentrate on the astrobiological factors that would not be seen by GAP - the oxidising properties of the near surface environment (such knowledge is also unlikely to be recovered easily by any future sample return mission). As such ESS attempts to quantify the existence of a local oxidising condition, oxidant production and transport. ESS investigates the local UV environment, to quantify a possible production mechanism [3], and measures the dust saltation rates (and the airborne dust loading via the camera) - a possible transport (storage) mechanism. Monitoring a simple *in situ* deposited silver film allows ESS to detect and quantify the oxidising capability of the air and regolith. One final astrobiological experiment, unrelated to oxidants, is the measurement of the total radiation dose over the mission lifetime. This characterization of the surface environment will also aid in the issue of the possibility of sub-surface life. Knowing the UV flux at the surface, it is possible to quantify UV penetration

into the regolith, especially when combined with surface analysis and imaging through the various instruments on Beagle 2.

Resources on the Beagle 2 lander are particularly scarce [6]. This has driven the overall mass budget for the seven chosen sensors of 153 grams. In some cases this has forced a move away from solutions based on designs with previous spaceflight heritage, in favour of commercial microtechnology-based solutions which are likely to have a higher associated risk of failure. However, this is compatible with the philosophy of the entire Beagle 2 design where cost and mass constraints have required an acceptance of risk throughout, including elimination of complete redundancy for mission critical systems.

Meteorology sub-system: Wind sensor This sensor is mounted on end of the robotic arm, such that it can be positioned at different heights and orientations. It is a hot film sensor, similar in concept to Viking and pathfinder instruments. It has been calibrated from 0-30m/s, although it will measure higher and further ground calibration remains to be done. Direction is measured to within to 10° .

Temperature sensor Air temperature is measured at 2 heights. One sensor is incorporated into the wind sensor, on the arm, and the second is located on the edge of one of the solar panel sheets, to minimize interference from the probe body. Expected absolute accuracy is 0.1K, with a resolution of 0.05K. Simultaneous measurements of temperature at two different heights can be used to estimate a vertical thermal profile.

Pressure Sensor This sensor is provided by the Finnish Meteorological Institute, based on a capacitive diaphragm design as flown on Mars-96. It has a range of 0-30mBar, with an absolute accuracy of 200 μ Bar and a resolution of 2 μ Bar.

Life environment sub-system: Radiation sensor This sensor is a RadFET, and provides a cumulative radiation dose information on the flux of high energy cosmic rays and solar protons at the Martian surface.

UV sensor Short wavelength UV, such as UVB and C are harmful to life, and can directly damage DNA. The UV environment on Mars is known to be harsh, and it is unlikely that life can survive on the surface, but subsurface life may still be possible. This sensor is a simple array of upward looking photodiodes with appropriate band-pass filters, giving a 5 point spectrum from 200-400nm. A 6th channel has no filter and provides aging information.

| Wavelength (nm) | Comment |
|-----------------|---|
| 210 | Main TiO ₂ dust absorption band |
| 230 | Biologically damaging and rapidly time varying regime |
| 250 | Secondary TiO ₂ band |
| 300 | Mid UVB |
| 350 | Mid UVA |
| Open channel | |

Table 1, detailing the UV sensor channels

Oxide sensor One controversial issue arising from the results from the Viking landers is the postulated presence of hydrogen peroxide (H₂O₂) or other oxidizing compounds in the soil, used in several cases to explain the results of the experiments designed to detect Martian life. This sensor deploys a thin silver film in situ by pulsed evaporation of a silver bead, and monitors the resistance of the film with time as it oxidizes. By repeated evaporations at different times of day, in conjunction with input from the cameras, the UV sensor and the onboard microscope, useful information will be obtained about the 'life cycle' of any oxidants present.

Additional sensors: Dust impact sensor Impacts from dust in the atmosphere of Mars will help to indicate how material is moved over the planet's surface. The sensor is a simple 50x50mm Al sheet, 0.25mm thick, with a piezoelectric film on the rear face. Minimum sensitivity is around 1×10^{-6} kgms⁻¹

Accelerometer Measurements of deceleration of the probe during the atmospheric entry and landing sequence can be used (in combination with the drag coefficient for the heat shield) to derive the upper atmosphere density and pressure. See for example Withers et al [7].

Two single axis sensors are used, with ranges of $\pm 30g$ and $\pm 10g$ on the probe axis. During the early entry phases pressure and density can be derived in upper atmosphere with an initial vertical resolution of 150m. Horizontal wind-speeds will be monitored during later descent after chute deployment, and the probe tilt once at rest will also be recorded.

Measurement Strategy: Throughout the surface-mission lifetime, each sensor will be sampled at a low rate, typically taking one reading from each sensor every 30 minutes. In addition to this, to study quickly changing conditions such as the dust devils seen by Viking[8] and Mars Pathfinder[9], the wind, temperature, pressure, and dust sensors will have a high sampling rate mode (1 per second), whereby data from the previous 5 minutes is buffered and only returned to earth (along with a further 5 minutes of data) should

any transient effects be detected. Of particular interest are dust devils, which may be the primary source of dust movement on Mars, and responsible for the homogeneity of the dust measured at the Viking and Pathfinder sites.

References: [1] R Schmidt et al, ESA Bulletin-European Space Agency, 1999, No.98, pp.56-66 [2] JC Bridges et al, JGR , 108 (E1): 5001, 2003 [3] AP Zent and C McKay, Icarus, 108, 146-157, 1994 [6] J Clemmet, ESA SP-468, 9-14, 2001 [7] P Withers et al, Planetary and Space Science, submitted. [8] For example, PP Thomas and P Gierasch, Science 230, 175-177, 1985. [9] JT Schofield, JR Barnes, D Crisp, RM Haberle, S Larsen, JA Magalhaes, JR Murphy, A Seiff, G Wilson, Science 278, 1752-1758, 1997

CONVECTIVE PLUMES AS ‘COLUMNS OF LIFE’. B. J. Travis, Los Alamos National Laboratory (EES-2/MS-T003, LANL, Los Alamos NM 87545; bjtravis@lanl.gov).

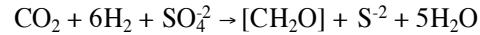
Introduction: A great deal of evidence supports the statement that water was abundant on Mars in its early history and that much of that inventory still exists today as ice and permafrost in the sub-surface, very likely with liquid water below that [1], [2]. A recent study [3] suggests that liquid water will be subject to widespread hydrothermal convection driven by the geothermal gradient, or the geothermal gradient augmented by magmatic intrusions. Subsurface convective flow patterns for Mars conditions are of the roll and plume types, with warm, upwelling plumes melting through the permafrost region and approaching closer to the surface and exhibiting higher upward flow rates than rolls (see Fig. 1). Water temperatures within upwelling plumes can range from 40 – 100 °C, at their base, to 0 – 10 °C at their top (even colder for saline solutions), depending on local heat flux and permeability structure of the host rock (see Fig. 2). These convective patterns are stable and long-lasting, and could provide a potential habitat for microbial life by bringing nutrients to and through microbial communities living in subsurface soil and rock. Upwelling plumes could function as ‘columns of life’. Further, for the higher geothermal heat fluxes of the past, flow will be episodic, characterized by occasional periods of enhanced flow rates and re-organization of the spatial arrangement of plumes, possibly providing a stimulus for evolution.

Fisk & Giovannoni [4] argue, based on the diversity of electron donor-acceptor mechanisms that microbial life on Earth has developed and on the similarities between the chemical and mineralogical make-up of Earth and Mars, that many chemolitho-autotrophic microbes that inhabit the Earth’s seafloor could likely survive in the Martian subsurface. Likely microbial candidates would include anaerobic thermophiles that utilize sulfur and carbon dioxide and iron, examples of which are found in abundance within mid-ocean ridge vent systems.

Microbes in Mid-Ocean Ridge Systems as Examples. In hydrothermal vents at mid-ocean ridges and other vent fields, there are many examples of microbes (mesothermophiles and hyperthermophiles) that utilize aerobic and anaerobic chemolithotrophic energy sources [5], typically in the temperature range 70 - 110 °C. These rely primarily on sulfur and hydrogen chemistry. There is evidence for interactions between thermophilic species. There are also examples of microbes (cryophiles) that can live in briny water inclusions in ice.

Some Anaerobic Energetic Reactions. Common reactions that provide energy for anaerobic thermophilic microbial metabolism on Earth include:

Sulfate reduction (e.g., *Archaeoglobus profundus*, at 90 °C)



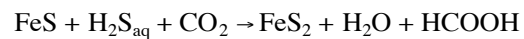
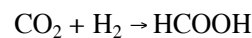
Methanogenesis (e.g., *Methanococcus igneus*, at 86 °C)



Denitrification (e.g., *Pyrobaculum sp.*, at 103 °C)



Another possible source of energy: pyrite formation



Simple Monod Model for Microbial Metabolism.

For a simple stoichiometry of the form



and assuming Monod (enzyme) kinetics for metabolic reactions, the following set of governing equations approximate transport, diffusion and reaction in the sub-surface:

$$\frac{\partial A}{\partial t} = -k M \frac{A}{K_A + A} \frac{B}{K_B + B} - \frac{1}{\alpha} \beta \cdot (VA) + D_A \nabla^2 A$$

$$\frac{\partial B}{\partial t} = -\alpha k M \frac{A}{K_A + A} \frac{B}{K_B + B} - \frac{1}{\alpha} \beta \cdot (VB) + D_B \nabla^2 B$$

$$\frac{\partial M}{\partial t} = \beta k M \frac{A}{K_A + A} \frac{B}{K_B + B} - k_d M$$

where A represents an electron donor (e.g., CH₄, H₂, H₂S), B is an electron acceptor (e.g., O₂, S, SO₄, NO₃, CO₂), M represents microbial biomass, K_i equals half-saturation and k equals max. utilization rate, V is Darcy velocity, α is porosity, D_i equals diffusivity, k_d is death rate of microbes.

Estimate of Growth Potential. Numerical solutions of the above equation set in general two and three dimensional settings, with even more complex metabolic models, are available [6]. Here, estimates of solutions will suffice. Making a steady state assumption, and assuming that B is in excess (B >> K_B), neglecting diffusion and assuming locally uniform flow, $A = K_A c / (1 - c)$, and $c = k_d / (\beta k)$, which implies that

$$M \sim (Q_A/L)/(c k) = V [A]_{\text{in}} / (\beta L k_d)$$

where [A]_{in} is the concentration of electron donor in fluid being entrained into a plume. Typical ranges of

values for the various coefficients for Earth-based microbes are: $\alpha = 0.33 - 0.50$, $K_A \sim O([A]_{in})$, $k_d \sim 10^{-4} - 10^{-1}$ /day, $\beta \sim 0.01 - 0.30$, $k \sim 10^{-2} - 10$ /day. Representative flow rate V in rolls and plumes for hypothetical hydrothermal convection on Mars [6] ranges from $2 \times 10^{-4} - 6.5 \times 10^{-3}$ m/day. This yields the estimates:

$M \sim 10^2 [A]_{in}/L$ for weak convection (rolls), and short-lived microbes

$M \sim 10^2 [A]_{in}/L$ for strong convection (plumes), hardy microbes

If $[A]_{in} \sim 10^{-5}$ g/cc and $L \sim 1,000$ m, then $M \sim 10^6$ g/cc which converts to about 10^6 microbes/cc in a plume.

Conclusions: Regions of warm to hot water should exist in the Martian subsurface (40-100 °C). The lower-lying northern plains are a more likely place for the fully saturated flow model assumed here, but if the H₂O inventory is sufficiently large, then the model may be applicable to parts of the southern hemisphere as well. Warm, flowing water in long-lasting upwelling plumes and convective rolls is capable of carrying dissolved minerals continuously to and through any microbial communities living within a hydrothermal convection system. Estimates of metabolic rates vs transport rates suggest that microbial life at concentration levels up to 10^6 g/cc (10^6 microbes/cc) might be sustainable over a spatial interval of 1,000 meters. Temperature structure within plumes provides a range of temperature zones and the chemical make-up could allow a series of life zones, ranging from habitations for thermophiles deep in the regolith at the base of plumes to mesophiles in the middle regions to cryophiles at plume tops. If plumes breached the surface occasionally, there could have been biomass residue deposited on the surface. There is also the possibility of seeps of very low concentrations of by-product gases such as methane.

Numerical simulation of convective patterns with reasonable values of controlling parameters such as geothermal heat flux and permeability structure and solubilities of various compounds, allows estimation of the maximum rate at which required substrates and nutrients could be delivered to any microbial communities living within convective plumes. When coupled to microbial metabolic models, these reactive transport simulations can provide an estimate of the possible size and spatial distribution of such communities.

References: [1] Clifford, S.M. (1993) *JGR* 98, 10973-11016. [2] Clifford, S.M. and T.J. Parker (2001) *Icarus* 154, 40-79. [3] Travis, B.J., N.D. Rosenberg, J.N. Cuzzi, in press, *JGR-Planets*. [4] Fisk, M.R. & S.J. Giovannoni (1999) *JGR* 104, 11805-11815. [5] Jannasch, H. W. (1995) in *Seafloor Hydrothermal Systems AGU Monograph 91*, 273-296. [6] Travis, B.J., N.D. Rosenberg (1997) *Environ. Sci & Tech.* 31, 3093-3102.

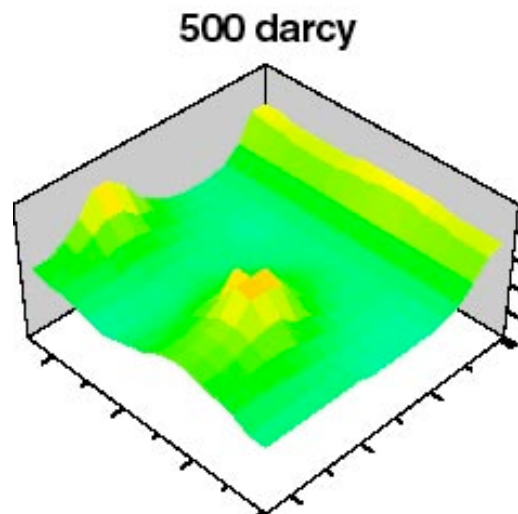


Figure 1. An example of pure-water subsurface hydrothermal convection under Mars-like conditions. Sides of box are 10 km each (vertical not to scale). Surface shown is the interface between underlying liquid water and overlying frozen soil, i.e., the 0 °C isotherm. The interface reflects the underlying regions of convective motion. The label '500 darcy' refers to surface value of permeability; permeability and porosity decrease exponentially from the surface down. Surface temperature is -60 °C and heat flux at the bottom is 40 mW/m².

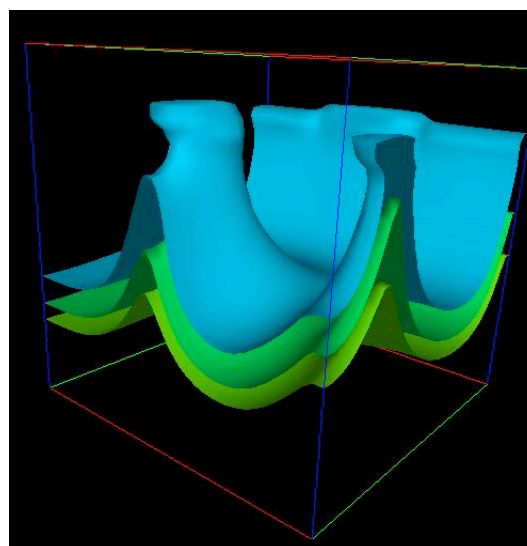


Figure 2. Temperature structure within hydrothermal convection plumes and rolls in the subsurface. Blue surface is the 10 °C isotherm, Green is 20 °C, and chartreuse is 30 °C. The box region is 10 km on a side. Basement temperatures can range from 40 to 100 oC depending on vigor of convection. Closeness of plume top to surface depends in part on salt content.